



An Integrated Synchronous Online Analyzer for Gaseous and Particulate Reactive Oxygen Species (ROS): Development, Characterization and Field Observations

Yihui Wang¹, Huan Song¹, Huabin Dong¹, Shiyi Chen¹, Linghan Zeng^{2*}, Keding Lu^{1*}

5 ¹State Key Laboratory of Regional Environment and Sustainability, International Joint Research Center for Atmospheric Research (IJRC), College of Environmental Sciences and Engineering, Peking University, Beijing, 100871, China

²State Key Laboratory of Atmospheric Environment and Extreme Meteorology, Institute of Atmospheric Physics, Chinese Academy of Sciences, Beijing, China

Correspondence to: Linghan Zeng (lhzeng@mail.iap.ac.cn), Keding Lu (k.lu@pku.edu.cn)

10 **Abstract.** An integrated online analyzer was developed for in situ, synchronous quantification of reactive oxygen species (ROS) in gaseous and particulate phases. Gaseous ROS (ROS_g) are absorbed by a glass spiral absorption tube, whereas particulate ROS (ROS_p) are collected at ambient temperature using a rotating wet annular denuder (WAD) for gas removal followed by a spray growth collection chamber. The collected solutions are analyzed using a fluorescence probe method, and the resulting fluorescent signal is recorded using a compact LED-PMT module (470/520 nm) and LabVIEW-based acquisition.

15 The system achieved high stability (RSD 0.37% over 10 h), fast tracking (7 min response), good repeatability (RSD 0.57%, $n=10$), and robust linearity ($y \approx 0.1x$, $R^2=0.99$) with detection limits of 0.07 ppbv (ROS_g) and 0.006 $\mu\text{g m}^{-3}$ (ROS_p) expressed as H_2O_2 equivalents. Field deployment in Beijing across four seasons revealed pronounced seasonal, diurnal, and pollution-regime dependence. ROS_g and ROS_p were highest in spring, while autumn exhibited the lowest levels despite severe $\text{PM}_{2.5}$ pollution. During humid autumn haze, enhanced aerosol water and secondary inorganic accumulation coincided with only

20 modest ROS_g growth and constrained ROS_p , indicating rapid multiphase turnover and efficient condensed-phase loss. In contrast, ozone-driven pollution in spring and summer strengthened photochemical production and gas-particle coupling, increasing ROS in both phases. Both ROS_g and ROS_p declined coherently during pollution clean-up, linking ROS variability to coupled changes in oxidation, partitioning, and removal.

1 Introduction

25 With the rapid acceleration of industrialization and urbanization, atmospheric pollution has become more complex and increasingly region-specific. Primary pollutants such as volatile organic compounds (VOCs), nitrogen oxides (NO_x), and sulfur dioxide (SO_2) are transformed through photochemical reactions and aerosol formation processes, thereby driving severe secondary pollution episodes (Liu et al., 2021). In China, this phenomenon is particularly evident, as secondary inorganic and organic aerosols often dominate fine particulate matter ($\text{PM}_{2.5}$), accounting for 40–60% of its total mass (Ying et al., 2024).

30 Although $\text{PM}_{2.5}$ levels have been substantially reduced in recent years by stringent emission control measures, surface ozone



(O₃) pollution has increased, emerging as a major challenge for air quality improvement (Guo et al., 2024). This shift reflects fundamental changes in the atmospheric oxidation capacity (AOC), which governs pollutant transformation, lifetime, and fate and thus plays a pivotal role in atmospheric chemistry and climate (Wang et al., 2023c).

Reactive oxygen species (ROS) are key carriers and indicators of AOC. Through complex radical chain reactions, ROS regulate the degradation of primary pollutants and the formation of secondary species, thereby shaping atmospheric self-cleaning capacity (Huang et al., 2016). ROS encompass a wide spectrum of oxidants, including radicals such as hydroxyl ($\cdot\text{OH}$), hydroperoxyl ($\text{HO}_2\cdot$), superoxide ($\text{O}_2\cdot^-$), and organic peroxy radicals ($\text{RO}_2\cdot$), as well as non-radical oxidants such as hydrogen peroxide (H_2O_2), organic hydroperoxides (e.g., methyl hydroperoxide, ethyl hydroperoxide, and peracetic acid) and singlet oxygen ($^1\text{O}_2$) (Lushchak and Lushchak, 2021). Their lifetimes range from microseconds to several days, with redox potentials between 1.3 and 2.8 V, resulting in phase-dependent chemical behaviors (Venkatachari and Hopke, 2008). In the gaseous phase, ROS such as $\cdot\text{OH}$ and $\text{HO}_2\cdot$ are short-lived yet remain central to photochemical oxidation. In the particulate phase, relatively stable peroxides such as H_2O_2 and organic peroxides can be adsorbed onto or embedded within $\text{PM}_{2.5}$ (Shiraiwa and Pöschl, 2021). These particles can reach the lungs, triggering endogenous ROS generation and oxidative stress, with potential health impacts (Venkatachari et al., 2007). Aqueous-phase ROS in cloud, fog, and rain droplets are produced via dissolution of gaseous species such as H_2O_2 and in situ photochemical reactions, driving multiphase oxidation and influencing AOC (Simões et al., 2021).

The formation and loss of atmospheric ROS are governed by interconnected processes across gaseous, particulate, and aqueous media. Gaseous ROS are primarily produced via O₃ and HONO photolysis, alkene ozonolysis, and radical interconversion reactions (Olague et al., 2009). In the particulate phase, transition-metal-catalyzed Fenton and Fenton-like reactions involving Fe²⁺/Fe³⁺ and Cu⁺/Cu²⁺ serve as major sources of $\cdot\text{OH}$ and $\text{O}_2\cdot^-$ (Charrier and Anastasio, 2012). Aqueous ROS are generated largely by self-reaction and ionization of $\text{HO}_2\cdot$ and its conjugate base $\text{O}_2\cdot^-$ in cloud water; the resulting H_2O_2 is an important oxidant for sulfur oxidation (Ervens et al., 2003). Conversely, ROS are depleted by reactions with NO_x and VOCs, photolysis, dry and wet deposition, and heterogeneous uptake on aerosol and surface films (George et al., 2013).

ROS not only initiate and propagate oxidation reactions, accelerating VOC and NO_x degradation and promoting O₃ formation (Lelieveld et al., 2008; Stone et al., 2012), but also contribute to sulfate, nitrate, and secondary organic aerosol (SOA) formation through heterogeneous and multiphase reactions (Wang et al., 2014; Li et al., 2018). Moreover, ROS-mediated oxidation can enhance aerosol hygroscopicity and aging, thereby altering cloud condensation nuclei (CCN) activity and radiative properties (Scott et al., 2014). Excessive ROS exposure also induces oxidative stress in biological systems, damaging proteins, lipids, and DNA and increasing risks of respiratory and cardiovascular diseases (Xie et al., 2023; Bates et al., 2015). Therefore, understanding ROS generation, transformation, and impacts is essential for elucidating atmospheric oxidation mechanisms and informing air quality management and climate mitigation strategies.



Accurate measurement of these species is therefore essential, yet remains methodologically challenging. Sampling techniques are phase-dependent: gaseous ROS are commonly sampled using cold trapping (Sakugawa and Kaplan, 1987; Hellpointner and Gäb, 1989; Campos and Kok, 1996), coil scrubbing (Lee et al., 1990; Lazrus et al., 1986), and membrane diffusion denuders (Huang et al., 2016; Allegrini et al., 1987), which enable efficient capture through low-temperature condensation, gas-liquid mass transfer, or selective permeation. In contrast, particulate ROS are typically collected using elution (Hung and Wang, 2001), spray capture (King and Weber, 2013; Zhou et al., 2018; Fuller et al., 2014), and steam condensation (Venkatachari and Hopke, 2008; Liu et al., 2023; Dong et al., 2012; Wu et al., 2022). These techniques employ aerosol mechanics such as vortexing or condensational growth into droplets for subsequent collection. For detection, fluorescence-based methods (e.g., DCFH-DA) are widely used due to their high sensitivity and real-time monitoring capabilities (Zhao and Hopke, 2012; King and Weber, 2013), though they may be susceptible to matrix interferences. Chemiluminescence (Yu and Zhao, 2021; Lakey et al., 2016; Zhang et al., 2018) and spectrophotometry (Jambunathan, 2010; Yang et al., 2020; Bielski et al., 1980) offer high sensitivity and ease of use but can be constrained in complex atmospheric matrices. More selective techniques like electron paramagnetic resonance (EPR) (D'errico et al., 2018; Mrakic-Sposta et al., 2012) and laser-induced fluorescence (LIF) (Fuchs et al., 2008; Zhang et al., 2025; Murakami et al., 2007) provide high sensitivity for specific ROS but are difficult to implement in field-deployable systems due to environmental susceptibility and specialized instrumentation requirements.

Despite significant advances, current atmospheric ROS measurement techniques continue to face several limitations. Gaseous ROS are often collected using rotating wet diffusion tubes, in which slow liquid renewal and signal averaging limit time resolution and hinder capture of transient variability. Particulate ROS sampling often relies on high-temperature vapor collection or prolonged mist capture, both of which can promote thermal decomposition or analyte loss. Moreover, fluorescence-based detection systems remain bulky and difficult to integrate, and synchronous online measurements of gaseous and particulate ROS are rarely available, hindering investigation of interphase interactions.

In this study, an atmospheric ROS online analyzer was developed and constructed as an integrated system for in situ quantification of gaseous and particulate ROS by coupling mild wet-chemical sampling with DCFH-based fluorescence detection. Instrument performance was systematically assessed and optimized via calibration and interference evaluation. The validated system was then deployed for field measurements in Beijing, enabling characterization of phase-dependent ROS levels and interphase coupling under contrasting pollution conditions and providing new constraints on atmospheric oxidation capacity and implications for precursor control strategies.



90 2 Instrument setup

2.1 Chemical reagents

2',7'-Dichlorodihydrofluorescein diacetate (DCFH-DA, $\geq 97\%$) was purchased from Aladdin, and horseradish peroxidase (HRP, ≥ 200 units mg^{-1}) was obtained from MREDA. Potassium dihydrogen phosphate (KH_2PO_4 , 99.5%), dipotassium hydrogen phosphate trihydrate ($\text{K}_2\text{HPO}_4 \cdot 3\text{H}_2\text{O}$, 99.0%), sodium hydroxide (NaOH, 97.0%), ethanol ($\text{CH}_3\text{CH}_2\text{OH}$, 99.8%), and hydrogen peroxide (H_2O_2 , 1000 $\mu\text{g mL}^{-1}$) were purchased from Macklin. All chemicals were of analytical grade, and deionized (DI) water was used for solution preparation. The phosphate buffer solution (PBS, pH 7.0) was prepared by mixing KH_2PO_4 and $\text{K}_2\text{HPO}_4 \cdot 3\text{H}_2\text{O}$ in DI water at appropriate ratios. To obtain the fluorescent reaction solution, DCFH-DA was dissolved in ethanol, hydrolyzed with NaOH for 30 min in the dark, and subsequently diluted with PBS to yield 10 $\mu\text{mol L}^{-1}$ 2',7'-dichlorodihydrofluorescein (DCFH). For the enzyme reaction solution, HRP was dissolved in PBS to a final activity of 2 units mL^{-1} . All reagents were stored at low temperature and protected from light.

2.2 Instrument principle

In this study, an online analyzer was developed to simultaneously quantify ROS_g and ROS_p using wet-chemical collection coupled with a fluorescence-probe assay. The instrument features two parallel systems, each composed of integrated sampling, delivery, reactor, and detection units, for real-time, in situ monitoring of both phases (Figure 1). For ROS_g , ambient air was first passed through a membrane filter to remove particles; the gaseous fraction was then absorbed into solution using a glass spiral absorption tube, followed by a gas-liquid separation chamber. The collected solution was mixed with the fluorescent probe and enzyme reagent in a premixing chamber and was subsequently derivatized at constant temperature in a reaction chamber prior to fluorescence detection. For ROS_p , $\text{PM}_{2.5}$ was size-selected using a cyclone, and residual ROS_g was removed by a rotating wet annular denuder (WAD). The remaining particles were collected in a spray growth collection chamber and transferred to the liquid phase for analysis, after which the same derivatization and detection steps as in the gaseous system were applied. A WAD was not used as a single-step phase separator because its large liquid holdup volume would lower the solution renewal rate and sensitivity, thereby degrading temporal resolution and smoothing short-term concentration variability.

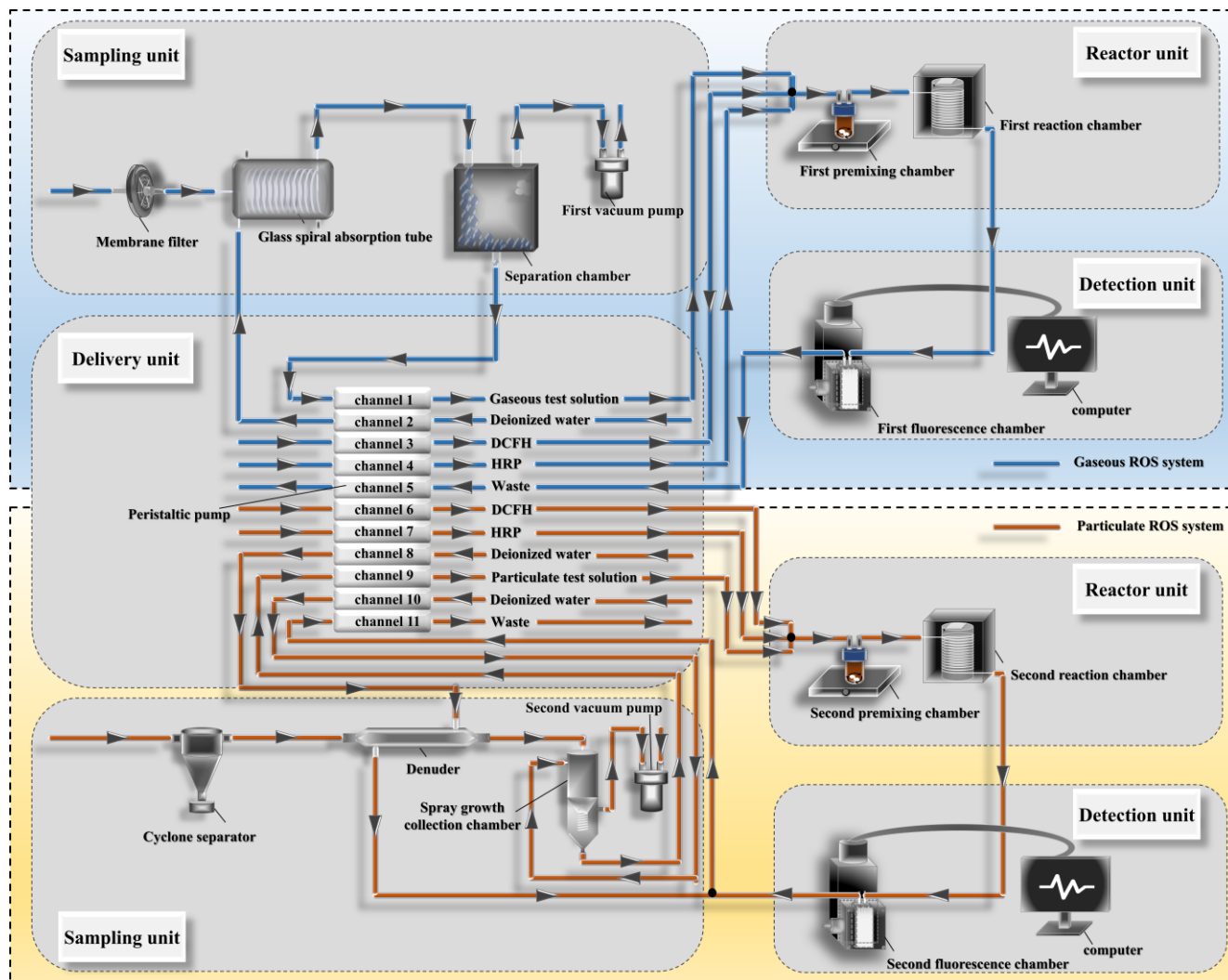
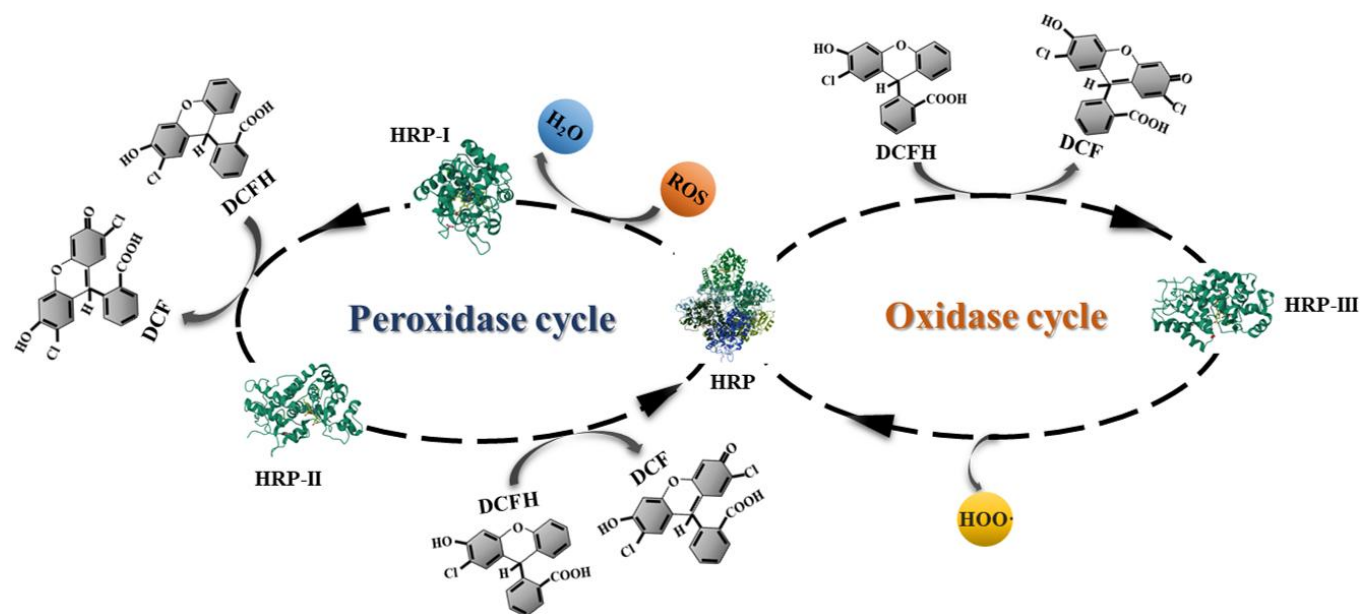


Figure 1. Overall operating flow path diagram of the instrument

115 The core principle of ROS quantification relies on the HRP-catalyzed oxidation of DCFH by ROS. As illustrated in Figure 2, ROS_g and ROS_p samples were first mixed with HRP. HRP was oxidized by ROS to form the active intermediate compound I (HRP-I). This intermediate then oxidized two DCFH molecules with weak native fluorescence to the highly fluorescent product DCF. Upon excitation at 470 nm, DCF emits fluorescence at 520 nm, and the signal intensity was proportional to the ROS concentration in the sample. Thus, ROS_g and ROS_p were quantified from the measured fluorescence signal.



120

Figure 2. Principle of the DCFH-HRP fluorescence method for ROS quantification

2.3 Instrument operation

The instrument operates via three integrated stages: sample collection, chemical derivatization, and optical detection. ROS in gas and particle phases are separately captured using wet absorption and spray growth collection chamber, then mixed online with DCFH and HRP to generate fluorescent products, enabling real-time, simultaneous measurement through a compact LED-PMT detection module.

125

2.3.1 Sample collection process

System flow is controlled by a peristaltic pump (Figure 1), and the flow rates and specific functions of each tubing line are summarized in Table S1. For ROS_g, ambient air is first passed through a membrane filter to remove ROS_p using the first vacuum pump (1 L min⁻¹), and is then introduced into a glass spiral absorption tube; its construction is shown in Figure S1. The tube comprises an inner glass spiral coil (2 mm i.d., 70 cm effective length) encased in an outer cylindrical glass shell (50 mm diameter, 100 mm height), with circulating-water inlets and outlets. In parallel, the absorbent is delivered at 1.0 mL min⁻¹ through a secondary line and introduced vertically at the same end of the tube. Surface tension maintains a stable liquid film along the spiral wall, allowing highly water-soluble ROS_g to be efficiently captured within ~0.13 s. A similar glass coil operated at 2 L min⁻¹ (gas) and 0.42 mL min⁻¹ (liquid) was reported to achieve a 99.8% collection efficiency for H₂O₂, supporting the adequacy of this configuration (Lazrus et al., 1986). The resulting solution is separated from the gas phase and delivered via channel 1 of the peristaltic pump to the first premixing chamber.

130

135

For ROS_p, ambient air is first size-selected by a cyclone driven by the second vacuum pump (16.7 L min⁻¹) and then directed



to a rotating WAD, where DI water serves as the absorbent solution. As the sample air enters the laminar inlet, ROS_g and ROS_p diffuse at different rates according to their molecular diffusivities, enabling selective uptake of ROS_g by the liquid film. Experimental evaluations showed that the rotating WAD achieved >98% removal efficiency for low-diffusivity gases such as SO₂ at concentrations below 200 μg m⁻³ (Dong et al., 2012). Consequently, ROS_p pass through the system unaffected and are transported into the spray growth collection chamber (Figure S2). Meanwhile, the absorbent solution is introduced perpendicularly via channel 10 of the peristaltic pump, and is accelerated through a nozzle by the Venturi effect to form a fine mist, providing ~0.3 s of growth time for aerosol particles. The high-speed airflow carries the particles to the chamber exit, achieving a 91.2% collection efficiency; the calculation procedure is provided in Supplement Materials (Text S1). The collected ROS solution is delivered to the second premixing chamber via channel 9 of the peristaltic pump, while the remaining gas is vented. Compared with conventional methods that rely on vapor introduction and cooling to promote particle growth, the ambient-temperature spray collection used in this study reduces thermally induced ROS decomposition. This temperature-moderated, water-based collection minimizes artifacts associated with steam-driven condensational sampling and preserves redox-labile ROS_p more effectively (Eftekhari et al., 2021). Rapid transfer into the aqueous phase also helps retain short-lived peroxide-like components that are prone to decomposition during high-temperature sampling or offline handling (King and Weber, 2013).

2.3.2 Chemical derivatization process

During the reaction process, the gaseous or particulate derivatization solution is delivered through channels 3, 4, 6, and 7 of the peristaltic pump, synchronized precisely with the solution-transport system. These flows are combined into a single stream using a three-way mixer and then are merged with the ROS_g or ROS_p analyte in a premixing chamber before entering the reaction chamber. Inside the reaction chamber (Figure S3), which is maintained at pH 7.0 and 40 °C, the ROS_g or ROS_p sample is derivatized with DCFH in the presence of HRP, generating the fluorescent product used for quantitative ROS determination.

2.3.3 Optical detection process

The fluorescent solution containing ROS_g or ROS_p is pumped continuously through a flow cell housed in the fluorescence detection chamber (Figure S4). A stable LED light source adjacent to the flow cell provides excitation at 470 nm, which is absorbed by the sample to induce emission at 520 nm. The emitted fluorescence is reflected by a planar mirror and then is passed through a 520 nm optical filter to suppress stray and scattered light before reaching the photomultiplier tube (PMT). At the PMT cathode, the optical signal is converted into a weak electrical current and is processed by an amplifier circuit for current-to-voltage (I/V) conversion. The resulting voltage signal is transmitted to the host computer via a data acquisition card (DAQ) and is recorded in real time using a self-developed LabVIEW program for stable, high-precision acquisition.

2.4 Instrument calibration

Calibration procedures were conducted using high-purity N₂ at flow rates exceeding sampling conditions to ensure system



170 stability. A series of H₂O₂ standard solutions and blank controls were introduced into the reaction chamber, and real-time signals were recorded via LabVIEW. The fluorescence response typically reached equilibrium within 10 min, after which data were collected for an additional 10 min to obtain steady-state averages. All measured ROS concentrations are expressed as H₂O₂ equivalents, representing relative rather than absolute quantification of ROS.

The concentrations of ROS_g and ROS_p in the sampling solutions were determined from voltage signals acquired in real-time using a LabVIEW program, following the relationship between fluorescence intensity and concentration:

$$I_a = KC_{ROS} - I_0 \quad (2.1)$$

where I_a is the measured fluorescence signal intensity, I_0 is the baseline intensity, and C_{ROS} is the concentration of ROS in the sampling solution ($\mu\text{g H}_2\text{O}_2 \text{ L}^{-1}$). The coefficient K was derived from the fluorescence intensities corresponding to standard H₂O₂ solutions.

180 The atmospheric concentration of ROS_g was calculated as:

$$C_{ROS_g} (\mu\text{g m}^{-3}) = \frac{C_{ROS} F_l}{F_g \gamma_g} \quad (2.2)$$

where C_{ROS_g} ($\mu\text{g m}^{-3}$) is the ROS_g concentration, F_l is the absorption liquid flow rate in the glass spiral absorber (1.0 mL min^{-1}), F_g is the gas sample flow rate (1.0 L min^{-1}), and γ_g is the collection efficiency of the glass spiral absorber for ROS_g. As the collection efficiency exceeded 99%, sampling losses were considered negligible.

185 The mass concentration was further converted to volumetric mixing ratios (ppbv) using:

$$C_{ROS_g} (\text{ppbv}) = \frac{C_{ROS} (\mu\text{g m}^{-3}) V_m}{M (T_0/T) (P_0/P)} \quad (2.3)$$

where V_m is the molar volume at standard conditions (22.4 L mol^{-1}), M is the molecular weight of H₂O₂ (34 g mol^{-1}), T_0 and P_0 are the standard temperature (273.15 K) and pressure (101.325 kPa), T and P are the ambient temperature and pressure during measurements.

190 The atmospheric concentration of ROS_p was calculated as:

$$C_{ROS_p} (\mu\text{g m}^{-3}) = \frac{C_{ROS} F_0}{F_g \gamma_p} \quad (2.4)$$

where C_{ROS_p} ($\mu\text{g m}^{-3}$) is the ROS_p concentration, F_0 is the collection liquid flow rate in the spray growth collection chamber



(1.0 mL min⁻¹), F_g is the sampling flow rate for ROS_p gas (16.7 L min⁻¹), and γ_p is the collection efficiency of the spray growth collection chamber. The value of γ_p was determined from recovery experiments based on three fractions: the collected chamber liquid (M_{col}), the wall-rinse solution obtained by washing the chamber and associated tubing to recover deposited material (M_{wall}), and the downstream backup filter-rinse solution used to quantify particle breakthrough (M_{filter}). For each fraction, the fluorescence response was measured under the same DCFH–HRP detection conditions and converted to an H₂O₂-equivalent amount using the corresponding calibration curve. The collection efficiency was defined as:

$$\gamma_p = \frac{M_{col} + M_{wall}}{M_{col} + M_{wall} + M_{filter}} \quad (2.5)$$

In the recovery test, 81.72% of the recovered amount was found in the chamber-collected liquid, 9.46% in the wall-rinse solution, and 8.80% on the downstream backup filter, yielding an overall collection efficiency of 91.2%. This value was therefore used to correct ROS_p concentrations in Eq. (2.4).

3. Instrument assessment

3.1. Parameter optimization

To enhance detection performance, systematic optimization of key parameters was conducted. This included reagent concentrations (DCFH and HRP), reaction temperature, and PMT/LED settings. Orthogonal experiments and systematic testing were performed to determine the optimal combination that maximizes fluorescence sensitivity, stability, and signal-to-noise ratio for reliable ROS quantification.

3.1.1 Reaction solution concentration

In the online detection of ROS_g and ROS_p, DCFH served as the fluorescent probe, while its oxidation product DCF exhibited fluorescence intensity positively correlated with ROS concentration. The derivatization reaction was catalyzed by HRP, thereby accelerating DCFH oxidation. To optimize reagent concentrations, an orthogonal experimental design was implemented with DCFH levels of 10.0, 20.0, and 40.0 μmol L⁻¹ and HRP levels of 0.5, 1.0, and 2.0 units mL⁻¹. Calibration curve slopes and baseline standard deviations (SD) were evaluated to quantify fluorescence sensitivity and measurement stability.

Results showed that increasing DCFH concentration enhanced fluorescence intensity by raising the abundance of reactive molecules (Table 1). However, excessively high DCFH concentrations led to higher background noise. For HRP, fluorescence intensity increased at first but decreased at higher concentrations. At 0.5-1.0 units mL⁻¹, DCFH was efficiently oxidized to DCF, whereas side reactions likely produced weakly fluorescent species, thereby reducing the net signal. When HRP was



220 increased further to 1.0-2.0 units mL⁻¹, the catalytic rate was enhanced, leading to increased DCF formation. Considering both signal intensity and stability, the optimal reagent composition was identified as 10.0 μmol L⁻¹ DCFH and 2.0 units mL⁻¹ HRP.

3.1.2 Reaction temperature

In practical applications, the usable activity window of HRP is constrained by its thermal stability. Previous studies have shown that HRP remains stable between 15 and 40 °C, whereas higher temperatures can cause irreversible denaturation (Ivanova et al., 2022; Abdulaal et al., 2020). In addition, the fluorescence quantum yield of DCFH shows a linear temperature dependence with a coefficient of -0.3% °C⁻¹ (Birks, 1976). Consequently, temperature fluctuations may counteract signal gains from faster enzymatic kinetics, resulting in nonlinear net responses. To identify suitable operating conditions, temperature-gradient experiments were conducted from 30 to 40 °C, within the favorable activity range of HRP. Calibration-curve slopes and baseline SD were analyzed to assess fluorescence response and measurement stability across temperatures.

230 As summarized in Table 1, the calibration-curve slopes varied only slightly (0.076–0.079), with R² values consistently above 0.99, indicating that HRP retained stable catalytic activity across the tested temperature range. In contrast, baseline SD decreased overall at higher temperatures and reached the lowest value at 40 °C. This trend may be attributed to faster molecular transport at higher temperatures, which enhances mixing and mass transfer and thereby reduces short-term signal fluctuations. Considering reaction completeness, measurement stability, and enzyme activity, 40 °C was selected as the optimal reaction temperature.

3.1.3 PMT high voltage and LED current

In the fluorescence detection system, the PMT high voltage directly determines signal gain. If the gain is set too low, weak fluorescence signals may remain undetected, whereas excessive gain can lead to signal over-amplification and increased noise. Likewise, the LED current controls excitation intensity, and deviations from the optimum can destabilize illumination, compromising signal reproducibility. Therefore, the combination of PMT high voltage and LED current was optimized to improve instrument sensitivity and the signal-to-noise ratio. To evaluate system stability, four PMT-voltage/LED-current combinations were tested; calibration-curve slope was used to represent response magnitude, and baseline fluctuations were quantified for each setting.

245 The evaluation results (Table 1) indicate that combination B (700 V–6 mA) provided the highest stability, with a baseline SD of 0.005, which was substantially lower than that of the other configurations. Combinations C (800 V–4 mA) and D (900 V–2 mA) showed slightly higher baseline SDs of 0.006, suggesting that higher PMT voltage can increase sensitivity but may also introduce additional noise. Combination A (600 V–8 mA) yielded the largest baseline SD (0.011), likely because the higher LED current increased device temperature and worsened long-term emission uniformity. Considering measurement stability and instrument longevity, combination B (700 V–6 mA) was selected as the optimal photodetector setting.



250 **Table 1.** Optimization of DCFH-HRP fluorescence detection conditions

Category	Parameter		Standard curve	Baseline SD
A. Reagent concentrations	c(HRP) (units mL ⁻¹)	c(DCFH) (μmol L ⁻¹)		
	0.5	10	y=0.068x; R ² =0.996	0.003
	0.5	20	y=0.080x; R ² =0.992	0.006
	0.5	40	y=0.093x; R ² =0.996	0.008
	1.0	10	y=0.063x; R ² =0.995	0.003
	1.0	20	y=0.072x; R ² =0.985	0.005
	1.0	40	y=0.080x; R ² =0.999	0.007
	2.0	10	y=0.089x; R²=0.996	0.002
	2.0	20	y=0.090x; R ² =0.992	0.009
2.0	40	y=0.096x; R ² =0.999	0.006	
B. Temperature effects	Temperature (°C)			
	30		y=0.076x; R ² =0.994	0.009
	33		y=0.078x; R ² =0.996	0.011
	37		y=0.078x; R²=0.998	0.005
40		y=0.079x; R ² =0.999	0.004	
C. Photoelectric detection effects	PMT voltage (V)	LED current (mA)		
	600	8	y=0.108x; R ² =0.996	0.011
	700	6	y=0.107x; R²=0.998	0.005
	800	4	y=0.105x; R ² =0.992	0.006
900	2	y=0.104x; R ² =0.995	0.006	

3.2. Performance assessment

To ensure accurate and reliable quantification of atmospheric ROS in both gas and particle phases, a comprehensive performance assessment was conducted (Table 2). This included tests of baseline stability, detection limits, reproducibility, sensitivity, response time, and linear working range. These evaluations confirm the instrument's suitability for long-term field deployment under complex atmospheric conditions.

3.2.1 Baseline Stability and Detection Limit

Baseline stability was evaluated by continuously recording the fluorescence signal of blank reagent for 10 h to quantify drift and assess long-term operational stability. Laboratory-grade DI water contains a steady-state background H₂O₂ concentration of up to ~60 nmol L⁻¹ due to equilibrium with dissolved oxygen, generating an inherent background fluorescence that defines



260 the instrumental baseline when DI water is used as the sample. As shown in Figure 3a, the signal remained within 0.927–0.953 V, corresponding to a total variation of 0.026 V. The SD and RSD were 0.0035 V and 0.37%, respectively, indicating stable baseline behavior during uninterrupted operation.

Baseline control is essential because reagent auto-oxidation can bias low-level ROS measurements. Dissolved oxygen promotes self-oxidation within the DCFH-HRP system, and DCFH is susceptible to photo-induced oxidation. These effects
265 were minimized using a fully light-shielded flow path and nitrogen protection of the reagent. In addition, peristaltic tubing wear can induce gradual flow attenuation and mixing-ratio changes, leading to baseline offset; thus, routine flow calibration and periodic tubing replacement are required.

The detection limit was derived using the 3σ criterion based on baseline noise, yielding 0.07 ppbv for ROS_g and $0.006 \mu\text{g m}^{-3}$ for ROS_p . These limits enable reliable quantification under low-background conditions and during routine ambient monitoring.

270 3.2.2 Reproducibility

Reproducibility was quantified using a $20 \mu\text{g L}^{-1}$ H_2O_2 standard measured repeatedly over 10 cycles. Standard solution and blank water were alternated to determine sample and background signals within each 16-min cycle, resulting in a total test duration of 160 min. As shown in Figure 3b, the mean peak-to-valley signal difference was 2.025 V with an RSD of 0.57%. The concentration confidence interval, expressed as three times the SD, was $(20.0 \pm 0.34) \mu\text{g L}^{-1}$, confirming consistent
275 instrument response over prolonged operation and across repeated reaction cycles.

3.2.3 Sensitivity and Response Time

Sensitivity was evaluated by alternating 10-min injections of H_2O_2 standard solution and 10-min injections of blank DI water to simulate rapid ambient variability. Standards of 5.0, 10.0, 20.0, and $25.0 \mu\text{g L}^{-1}$ correspond to ROS_g of 2.88, 5.76, 11.52, and 14.41 ppbv, and ROS_p of 0.29, 0.59, 1.19, and $1.49 \mu\text{g m}^{-3}$. Each level was tested in triplicate. The response time (T_{90}),
280 defined as the time required to reach 90% of the final signal change, was consistently 7 min for both signal increases and decreases (Figure 3c), demonstrating rapid tracking of concentration transitions across the tested range.

3.2.4 Linear Working Range

The linear working range was determined by simultaneous injection and switching tests in the gas and particle phase channels using the same H_2O_2 standards ($5.0\text{--}25.0 \mu\text{g L}^{-1}$). Regression analysis showed a strong linear relationship between fluorescence
285 intensity and standard concentration, with a near-zero intercept calibration of $y \approx 0.1x$ and $R^2 = 0.99$ (Figure 3d). The two channels exhibited nearly identical linear ranges, trends, response times, and calibration slopes, indicating strong inter-channel agreement and stable system matching. The RSD at each concentration point was below 1%, supporting robust quantitative performance. The atmospheric-equivalent concentration coverage ($2.88\text{--}14.41$ ppbv for ROS_g and $0.30\text{--}1.49 \mu\text{g m}^{-3}$ for ROS_p)



290 satisfies the requirements for ambient measurements, with the established linear calibration range being generally suitable for practical atmospheric observations.

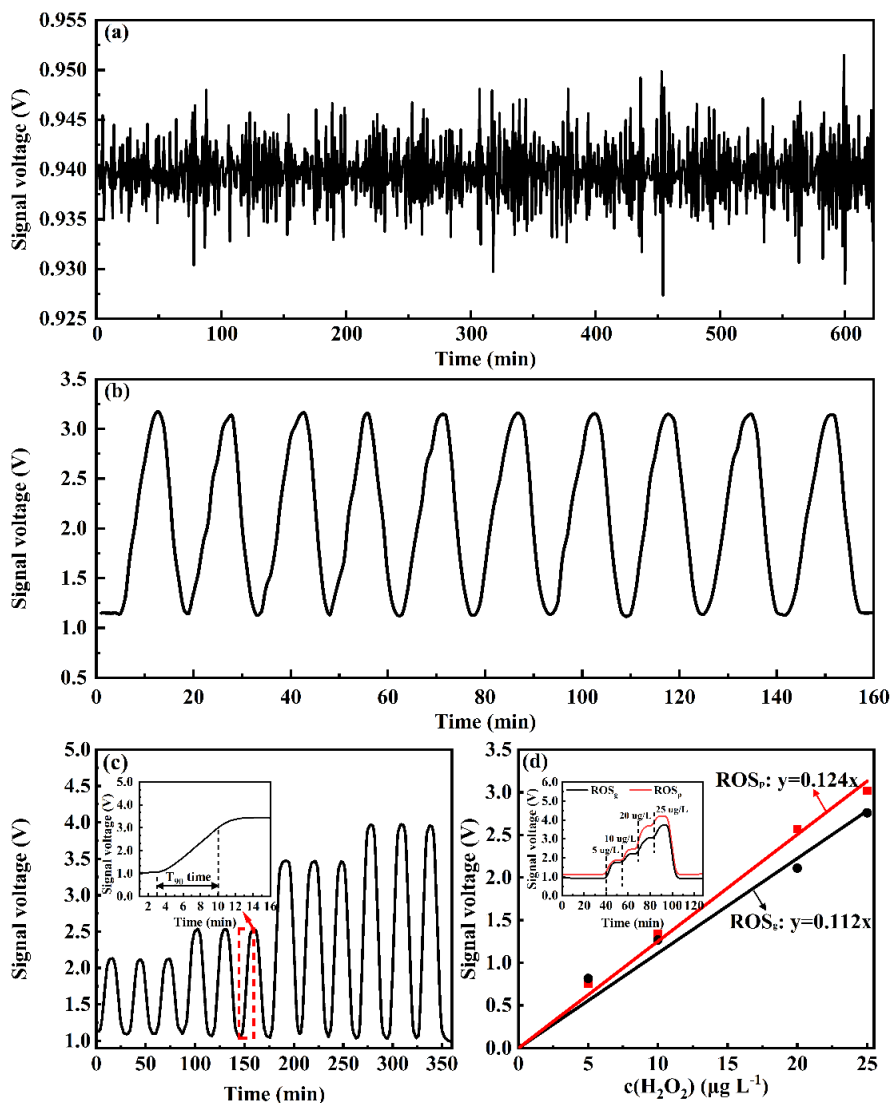


Figure 3. Performance evaluation of the atmospheric ROS online analyzer: (a) baseline stability, (b) reproducibility, (c) sensitivity, and (d) linear working range.

Table 2. Performance specifications of the atmospheric ROS online analyzer

Parameter	Test Method / Condition	Result
Baseline Stability	Continuous operation for 10 hours	RSD: 0.37%
Limit of Detection (LOD, 3σ)	ROS _g	0.07 ppbv



	ROS _p	0.006 μg m ⁻³
Response Time	Switching between standards and blank	7 min
Repeatability	10 replicate injections of 20 μg L ⁻¹ H ₂ O ₂	RSD: 0.57%
Linear Range	Regression Equation	y≈0.1x (R ² =0.99)

295 3.3. Interference assessment

This instrument quantifies ROS_g and ROS_p based on their water solubility using wet-chemical collection coupled with fluorescence probes. In ambient measurements, however, coexisting soluble species, including O₃, NO_x, SO₂, and transition metal ions, may interact with target analytes or participate in side reactions, potentially biasing the quantification of atmospheric ROS.

300 For oxidizing gases, O₃ interference exhibits a pronounced concentration dependence. At typical ambient levels near 40 ppbv, the dissolved O₃ concentration estimated from Henry's law is 0.27–0.36 nmol L⁻¹, which is insufficient to cause measurable interference in DCFH-based ROS detection (Huang et al., 2016). Laboratory experiments further demonstrated that O₃ at 60–80 ppbv induced negligible responses in DCFH systems, indicating limited influence under realistic atmospheric conditions (King and Weber, 2013). Field evaluations showed that even at 100 ppbv O₃, the maximum error in H₂O₂ quantification was
 305 below 0.03 ppbv, consistent with previous observations (Lee et al., 1995; Lazrus et al., 1986). In contrast, under extremely elevated O₃ levels up to 470 ppbv, dissolution-driven reactions can generate secondary ROS, including ·OH, H₂O₂, and HO₂·, which introduce positive artifacts and compromise the representativeness of measured ROS concentrations (Montesinos et al., 2015).

For reducing gases, NO can induce a weak negative bias by consuming H₂O₂. The addition of 130 ppbv NO to 0.53 ppbv H₂O₂
 310 resulted in a signal decrease of 0.016 ppb (Lazrus et al., 1986). Given that ambient NO concentrations are typically much lower and H₂O₂ levels are often elevated during polluted conditions, this effect is negligible for ambient applications. SO₂ interference displays strong concentration and pH dependence. Experimental studies reported H₂O₂ signal losses of 10%, 30%, and 50% at SO₂ concentrations of 10, 25, and 50 ppbv, respectively, whereas organic hydroperoxides exhibited lower sensitivities (Hua et al., 2008). Additional studies showed that SO₂-induced negative bias increases at lower pH due to
 315 accelerated S(IV)-H₂O₂ reaction kinetics (Komazaki et al., 2001; Tanner et al., 1986). In fluorescence-based H₂O₂ detection, SO₂ can interfere with fluorophore formation through acid-catalyzed reactions. This interference can be fully suppressed by adding formaldehyde, which scavenges dissolved SO₂ through the formation of a stable HCHO-SO₂ adduct, thereby ensuring accurate H₂O₂ quantification even under elevated SO₂ conditions (Lazrus et al., 1986).

Interference from transition metal ions depends on their oxidation state and chemical speciation. Soluble Fe²⁺ at
 320 environmentally relevant levels of approximately 1 nmol L⁻¹ does not affect ROS signals, whereas elevated Fe²⁺ concentrations



can consume H_2O_2 and suppress fluorescence. In contrast, Fe^{3+} exhibits no detectable interference, consistent with previous studies (Keenan et al., 2009; Lebel et al., 1992). Cross-tests using extracts from rural and urban aerosol filters further indicate that complex particulate matrices do not significantly influence ROS signals at atmospherically relevant concentrations (Zhou et al., 2018).

325 4. Field Observations of Seasonal ROS Concentrations

4.1. Observation Methods

Field observations of ROS_g and ROS_p were conducted using the atmospheric ROS online analyzer at the observation site in Beijing (116.31 °E, 39.99 °N) during four seasons: autumn (October 29–November 15, 2024), winter (December 10–31, 2024), spring (April 24–May 15, 2025), and summer (June 13–July 5, 2025). In addition to ROS measurements, routine atmospheric
330 pollutants were continuously monitored in real time. O_3 was monitored using a Model 49i ozone analyzer (Thermo Fisher Scientific, USA), while NO_x and SO_2 were measured with Model 42i and Model 43i-TLE analyzers, respectively (Thermo Fisher Scientific, USA). $\text{PM}_{2.5}$ mass concentration was determined using a TH-2000Z1 monitor (Tianhong, China). Photolysis frequencies, including $j(\text{O}^1\text{D})$, $j(\text{HONO})$, and $j(\text{H}_2\text{O}_2)$, were derived from actinic flux spectra recorded over 280–650 nm using a UF-CCD spectroradiometer (MetCon, Germany) followed by spectral inversion. HONO, NH_3 , and HNO_3 were quantified
335 using a gas aerosol collector-ion chromatography (GAC-IC) system (Peking University, China). VOCs were measured by ZF-PKU-VOC1007 system (Pengyu Changya, China), and non-refractory components in submicron aerosol particles were characterized by ToF-ACSM (Aerodyne Research, USA).

Observation days were classified as polluted days when the daily maximum 8-hour average O_3 concentration exceeded $160 \mu\text{g m}^{-3}$, corresponding to a mixing ratio of ~ 80 ppbv, or when the 24-hour average concentration of $\text{PM}_{2.5}$ and PM_{10} exceeded $75 \mu\text{g m}^{-3}$ and $150 \mu\text{g m}^{-3}$, respectively. Days that did not meet any of these criteria were defined as clean days.
340

4.2. Overall variations of ROS and associated atmospheric species

Figure 4 presents the seasonal and pollution-dependent variations of ROS and associated atmospheric species, and the corresponding seasonal statistics under clean days (CDs) and polluted days (PDs) are summarized in Table S2. Notably, the seasonal-mean ROS_g peaked in spring (2.28 ppbv) and was lowest in autumn (1.03 ppbv), whereas ROS_p was highest in spring
345 ($0.45 \mu\text{g m}^{-3}$) and lowest in autumn ($0.15 \mu\text{g m}^{-3}$). A broader comparison with previous field observations is provided in Figure 5 and Table S3. As summarized there, reported atmospheric ROS levels span a wide range across regions and seasons, although part of the gas-phase dataset used for comparison is derived from measurements of gaseous H_2O_2 alone. Within this observational context, the ROS_g levels measured in this study are generally at the upper end of previously reported urban observations, whereas ROS_p falls within the range of earlier measurements and remains at a moderate level relative to the most
350 elevated reported values. Specifically, the seasonal-mean ROS_g (1.03 – 2.28 ppbv) exceeds most reported values for urban



Beijing and several other Asian sites, while remaining comparable to observations at photochemically active continental locations. In contrast, the seasonal-mean ROS_p ($0.15\text{--}0.45\ \mu\text{g m}^{-3}$) is broadly comparable to previous urban measurements, but lower than the highest values reported for highly oxidized particulate environments. Overall, these comparisons indicate that the present observations were characterized by relatively elevated ROS_g but moderate ROS_p , highlighting a distinct phase-
355 dependent distribution of atmospheric oxidative burden in urban Beijing.

In autumn, pollution was primarily characterized by $PM_{2.5}$ accumulation under humid and weakly dispersive conditions. Compared with clean days, polluted days exhibited a near threefold increase in $PM_{2.5}$ (94.88 vs $33.45\ \mu\text{g m}^{-3}$), accompanied by higher RH (78% vs 67%) and lower wind speed (1.19 vs $1.68\ \text{m s}^{-1}$) (Table S2). These meteorological features favor pollutant accumulation and enhance multiphase processing, consistent with the elevated ROS_g from 0.89 ppbv on CDs to 1.34
360 ppbv on PDs. By contrast, ROS_p showed no corresponding increase (0.16 vs $0.13\ \mu\text{g m}^{-3}$), suggesting that particle-phase oxidative activity in autumn was not directly proportional to $PM_{2.5}$ mass, but was instead constrained by the competing effects of ROS formation and depletion under humid, stagnant conditions (Campbell et al., 2021).

During winter, ROS_g (1.22 ppbv) and ROS_p ($0.23\ \mu\text{g m}^{-3}$) exceeded autumn despite weak photolysis, consistent with the seasonally highest SO_2 and strengthened combustion-related emissions. Enhanced residential coal burning for heating can
365 increase primary oxidant inputs and elevate the fractions of black carbon and redox-active metals in $PM_{2.5}$. These components promote secondary inorganic production and provide abundant reactive surface area and condensed-phase microenvironments that facilitate heterogeneous and multiphase processing, thereby sustaining ROS_p and indirectly supporting ROS_g via gas-particle partitioning and multiphase recycling even under weak winter radiation (An et al., 2019; Song et al., 2024).

In spring, ROS_g exhibited a marked enhancement from 2.10 ppbv on CDs to 3.02 ppbv on PDs, coinciding with sharp increases
370 in O_3 ($39.35\text{--}60.21$ ppbv) and $j(O^1D)$ ($4.52\times 10^{-6}\text{--}7.13\times 10^{-6}\ \text{s}^{-1}$), indicative of O_3 -driven photochemical pollution. Notably, ROS_p in spring remained comparably high on both CDs and PDs ($0.45\ \mu\text{g m}^{-3}$), implying that once photochemistry becomes sufficiently strong, particle oxidative activity can be sustained even under relatively lower aerosol loading, potentially through continued production and uptake of peroxides and other semi-volatile oxidants and in-particle transformation pathways (Huang et al., 2016; Zhou et al., 2019).

375 Summer featured the strongest photochemical environment, with O_3 approaching 61 ppbv and $j(O^1D)$ reaching about $1.0 \times 10^{-5}\ \text{s}^{-1}$. ROS_g increased modestly from 1.04 to 1.29 ppbv from CDs to PDs, while ROS_p showed a pronounced enhancement ($0.24\text{--}0.41\ \mu\text{g m}^{-3}$). High temperatures ($\sim 302\ \text{K}$) enhance biogenic isoprene abundance (0.16 ppbv) and accelerate its oxidation kinetics, leading to increased RO_x production (Wennberg et al., 2018). Meanwhile, isoprene-driven SOA formation supplies peroxide-rich and low-volatility products to particles, boosting ROS_p concentration and yielding a larger ROS_p response than
380 ROS_g (Zhou et al., 2019; Enami, 2021; Kroll et al., 2006).

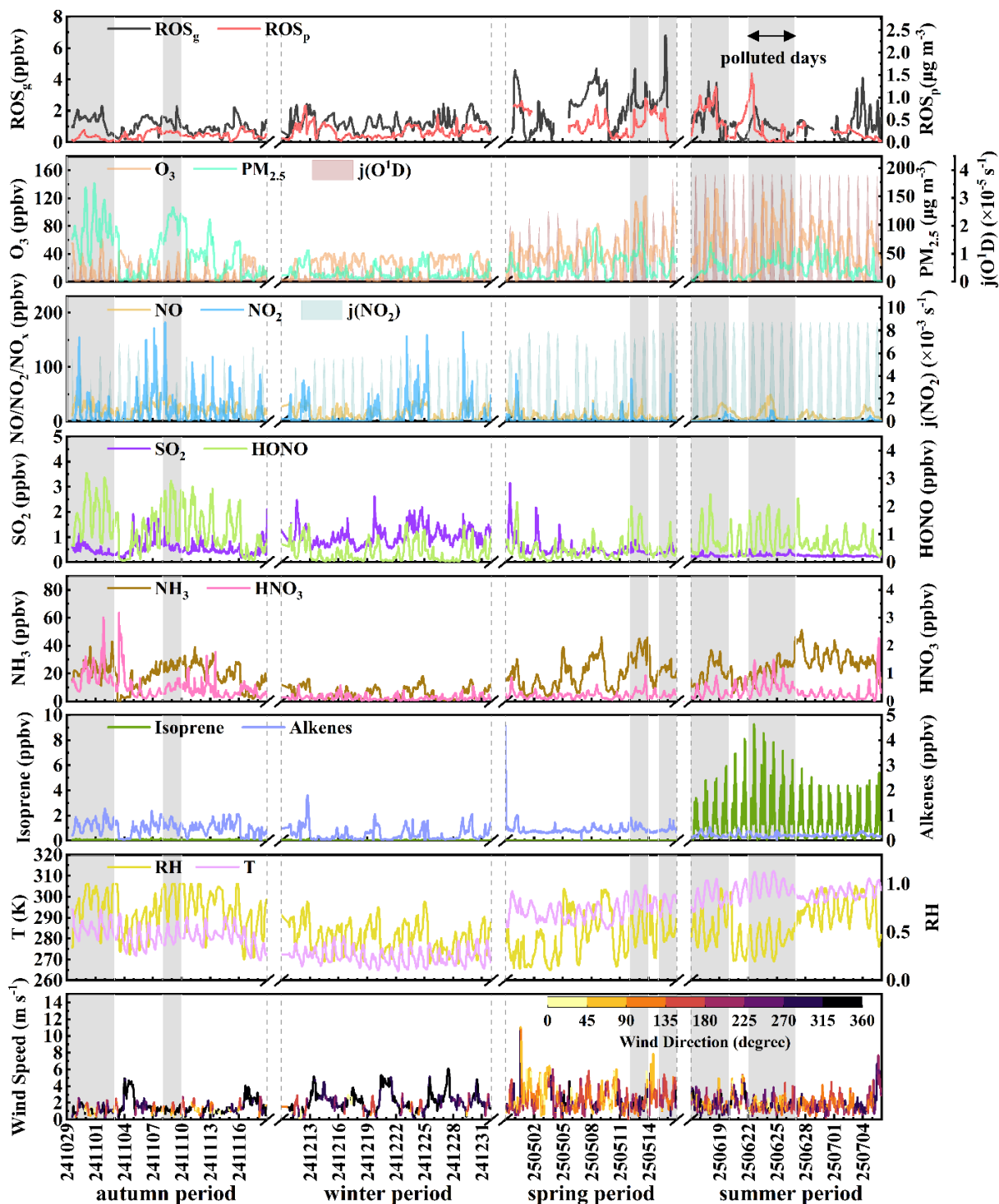
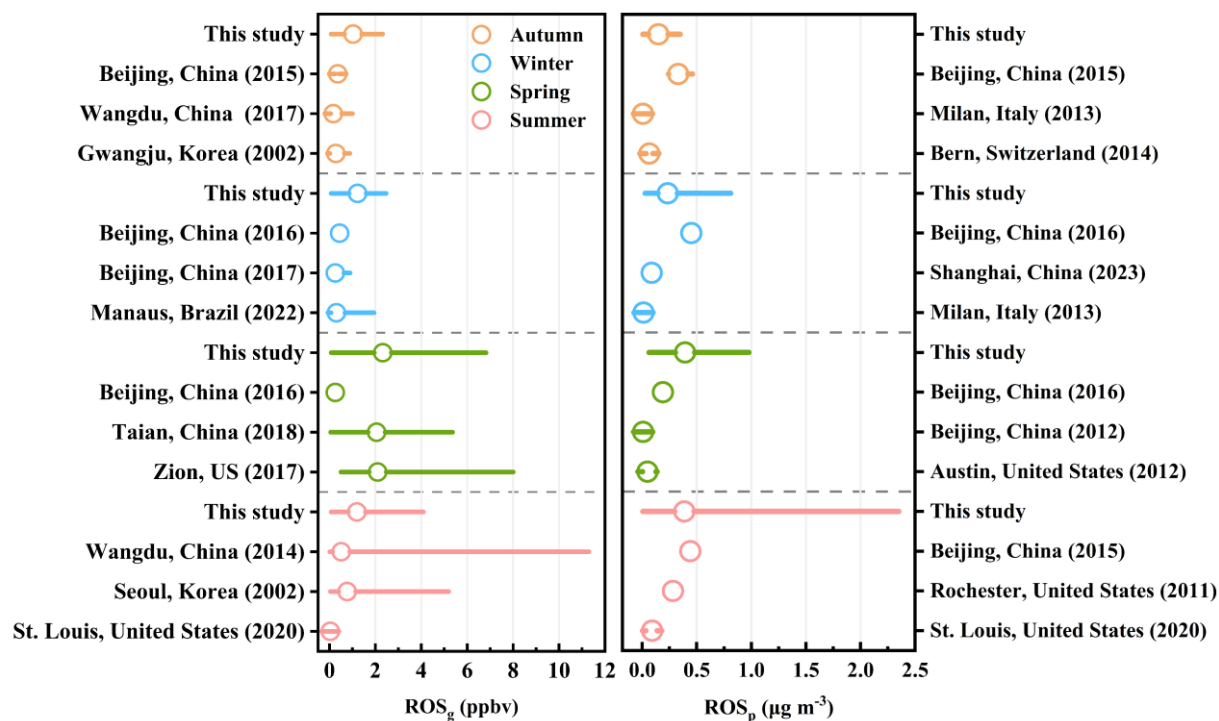


Figure 4. Temporal variations of ROS and related atmospheric constituents during the observation period



385 **Figure 5.** Comparison of seasonal mean ROS_g and ROS_p concentrations observed in this study with those reported in previous field observations from different regions. Circles denote mean values, and horizontal lines denote the corresponding concentration ranges. All concentrations are expressed as H_2O_2 equivalents; literature data were converted to ppbv for ROS_g and $\mu g m^{-3}$ for ROS_p where applicable. Detailed data sources are summarized in Table S3.

4.3. Diurnal patterns of ROS under clean and polluted conditions

390 Across all seasons, the diurnal evolution of ROS reflected the combined influence of photochemical intensity, precursor availability, and boundary-layer dynamics, with clear contrasts between gas-phase and particle-phase behavior under clean (Figure 6) and polluted conditions (Figure 7). Overall, ROS_g was primarily regulated by daytime photochemical production and nighttime regeneration, whereas ROS_p integrated the cumulative effects of gas-particle partitioning of oxidized products and multiphase oxidation, leading to distinct phase-dependent diurnal responses.

395 From late morning to early afternoon (08:00–15:00), photochemical processes dominated ROS evolution. ROS_g increased markedly with rising O_3 and photolysis activity, reflecting rapid expansion of the daytime oxidative pool involving HO_x - RO_x radicals and peroxides (Stone et al., 2012; Nosaka and Nosaka, 2017; Liu et al., 2023). Under clean conditions, ROS_g and ROS_p exhibited distinct responses, particularly in autumn (Figure 6a). ROS_g showed a weak negative correlation with O_3 in clean autumn air ($r = -0.15$) (Figure 8), suggesting stronger effects of titration and precursor limitation in relatively clean air masses. Meanwhile, reactions between O_3 and alkenes may generate Criegee intermediates, promoting SOA formation and secondary ROS production (Chen et al., 2011; Yao et al., 2014). In contrast, ROS_p generally peaked earlier than ROS_g and

400



showed a strong positive association with NO under clean autumn conditions ($r = 0.60$) (Figure 8), indicating close coupling with fresh NO_x-influenced air masses. Under polluted conditions, daytime ROS_p was more clearly decoupled from bulk particle loading. In polluted autumn (Figure 7a), the weak correlation between ROS_p and PM_{2.5} ($r = 0.28$) suggests that ROS_p was governed more by aerosol composition and secondary processing than by total particle mass, consistent with previous studies (Liu et al., 2023; Zhou et al., 2019; Huang et al., 2016). At the same time, the positive association between ROS_p and NO weakened relative to clean conditions ($r = 0.46$) (Figure 8), indicating a reduced influence of fresh emissions and a greater contribution from secondary formation processes.

During the late afternoon and early evening (15:00-20:00), seasonal contrasts became more pronounced. In spring polluted conditions (Figure 7b), ROS_g continued to increase until late afternoon, whereas ROS_p declined after its midday maximum. In summer, ROS_g generally peaked later in the day, whereas ROS_p peaked earlier under polluted conditions (Figure 7c) but remained relatively stable under clean conditions (Figure 6d). Under clean summer conditions (Figure 8), ROS_p showed moderate negative correlations with NO ($r = -0.40$) and NO₂ ($r = -0.39$), indicating suppression of ROS_p accumulation by fresh NO_x, while ROS_g was positively correlated with NO ($r = 0.36$) and negatively correlated with O₃ ($r = -0.22$), reflecting competition between titration and photochemical regeneration (Zhou et al., 2019; He et al., 2022). In autumn, delayed ROS_g maxima relative to O₃, together with positive associations with PM_{2.5} ($r = 0.28$) under polluted conditions (Figure 8), suggest that gas-particle coupling, boundary-layer transport, and O₃-alkene reactions continued to sustain oxidative capacity after peak photochemistry (Wang et al., 2023b). In winter, declining ROS_g and weakly rebounding ROS_p in the evening, along with positive associations of ROS_p with PM_{2.5} ($r = 0.22$) (Figure 8), highlight the increasing importance of heterogeneous oxidation as photochemical activity wanes (Xue et al., 2021).

From evening through early morning (20:00-08:00), boundary-layer stabilization favored nocturnal accumulation and phase repartitioning, while oxidant production was increasingly regulated by nighttime chemistry and post-sunrise reactivation. In autumn polluted conditions (Figure 7a), ROS_p typically reached an early-evening maximum and then remained elevated, whereas ROS_g declined after dusk but rebounded toward midnight; this nocturnal increase is plausibly linked to NO₃-driven oxidation, peroxide decomposition, and ozonolysis of alkenes, which can sustain nighttime radical recycling and replenish the gas-phase oxidative pool (Venkatachari and Hopke, 2008). Under clean winter and spring conditions (Figure 6b and 6c), ROS_g showed weak nocturnal variability, while ROS_p generally decreased in colder seasons but persisted or increased in summer with weak PM_{2.5} dependence ($r = 0.12$) (Figure 8), indicating sustained multiphase ROS formation without strong photochemical forcing (Brown and Stutz, 2012; Wang et al., 2023a). After midnight, ROS_g in autumn continued to decrease toward sunrise under both clean (Figure 6a) and polluted conditions (Figure 7a), and under clean conditions it tracked NO ($r = 0.36$) (Figure 8), implying precursor-driven background control under weak radiation (King and Weber, 2013; Nan et al., 2017). Under clean winter conditions, ROS_g showed limited variability and only weak associations with NO and NO₂ ($r = 0.06$ – 0.11), whereas ROS_p correlated more strongly with PM_{2.5} ($r = 0.22$) (Figure 8), underscoring the sustained contribution



of nocturnal heterogeneous and aqueous-phase oxidation (Liu et al., 2023; Campbell et al., 2021). In spring and summer, ROS_g more frequently rebounded or increased in the early morning, particularly under polluted conditions, suggesting enhanced oxidative activity after sunrise. 435

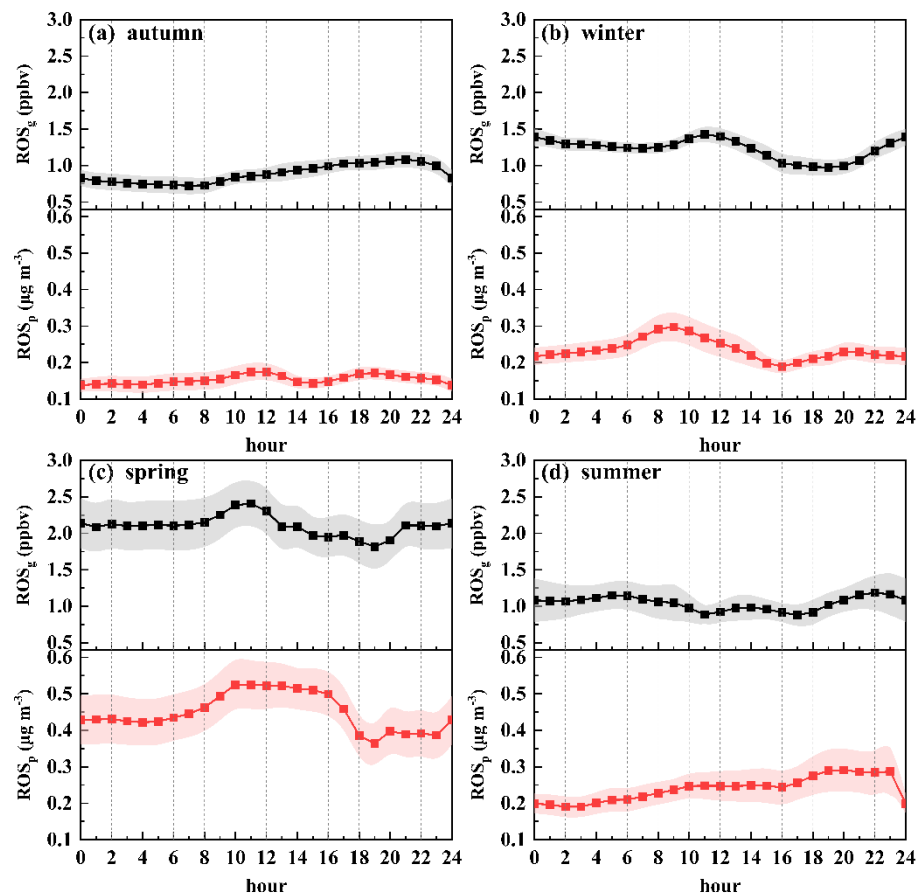


Figure 6. Seasonal diurnal profiles of ROS_g and ROS_p in clean days

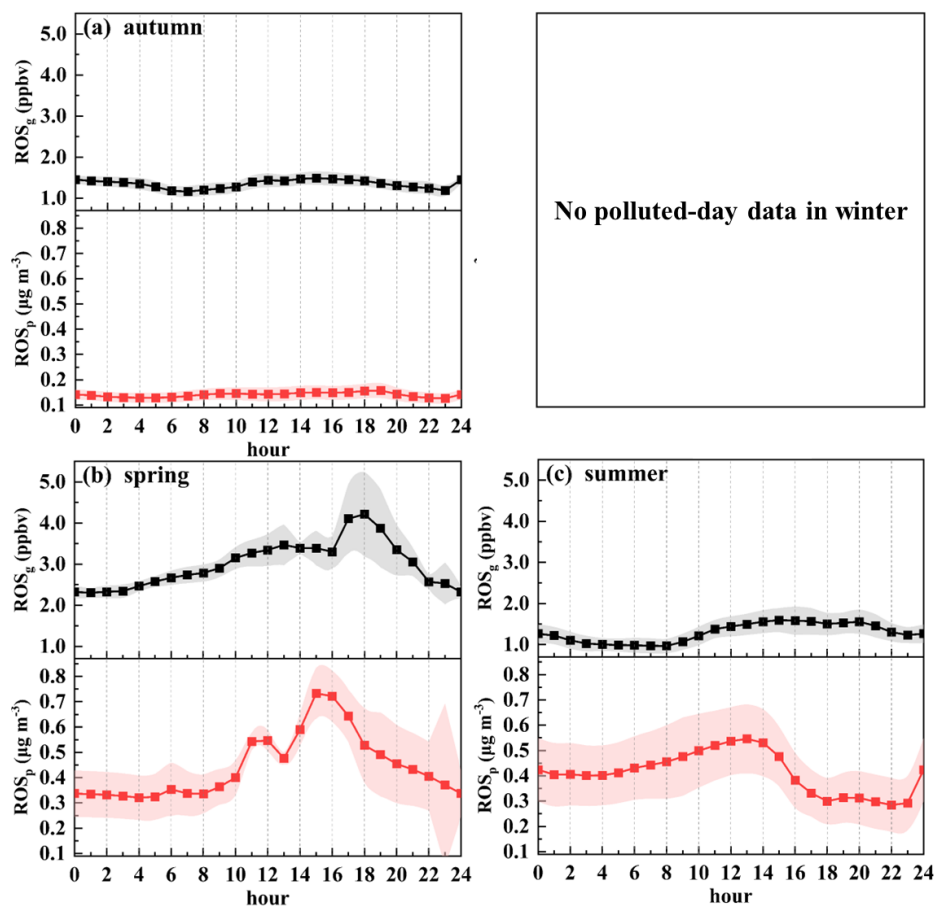


Figure 7. Seasonal diurnal profiles of ROS_g and ROS_p in polluted days

	autumn				winter		spring				summer			
	clean days		polluted days		clean days	polluted days	clean days		polluted days		clean days		polluted days	
ROS_g	1	0.3	1	0.37	1	0.39	1	0.31	1	0.21	1	-0.38	1	0.6
ROS_p	0.3	1	0.37	1	0.39	1	0.31	1	0.21	1	-0.38	1	0.6	1
O_3	-0.15	0.14	0.28	-0.06	-0.058	-0.18	-0.055	-0.075	0.26	0.45	-0.22	0.12	0.17	-0.19
$PM_{2.5}$	0.14	0.021	0.036	0.14	0.23	0.22	0.39	-0.19	-0.51	-0.28	0.035	-0.12	-0.042	-0.31
NO	0.36	0.1	0.18	0.46	0.063	0.19	0.35	0.048	-0.36	-0.58	0.36	-0.4	-0.17	-0.29
NO ₂	0.16	0.051	0.098	0.096	0.11	0.2	0.25	0.14	-0.15	-0.36	0.15	-0.39	-0.25	-0.33
	ROS_g	ROS_p	ROS_g	ROS_p	ROS_g	ROS_p	ROS_g	ROS_p	ROS_g	ROS_p	ROS_g	ROS_p	ROS_g	ROS_p

440

Figure 8. Seasonal correlations of ROS_g and ROS_p with key atmospheric species



4.4. Variations of ROS during typical pollution episodes

Based on the time series (Figure 9) and clustered back trajectories (Figure S5), the three representative episodes can be classified into two contrasting ROS regimes: an aerosol water-driven multiphase regime in autumn and photochemically driven oxidation regimes in spring and summer. Across all episodes, ROS_g generally increased during pollution development, whereas ROS_p showed episode-dependent behavior. Aerosol liquid water content (ALWC) and particle pH estimated by ISORROPIA-II provide a consistent thermodynamic framework for interpreting the coupled evolution of aerosol water, acidity, and semi-volatile partitioning (Fountoukis and Nenes, 2007). The HYSPLIT back trajectories further suggest seasonally distinct transport patterns that modulated precursor supply and ventilation efficiency, thereby influencing ROS formation and removal (Stein et al., 2015; Draxler and Hess, 1998, 1997).

The autumn episode was characterized by $PM_{2.5}$ -dominated pollution, with the highest ALWC and the strongest coupling of $PM_{2.5}$ with aerosol water and secondary inorganic aerosols, especially nitrate (Figure 8). During this period, ROS_g increased modestly from 0.89 to 1.34 ppbv, whereas ROS_p slightly decreased from 0.16 to 0.13 $\mu g m^{-3}$, and both remained lower than in spring and summer (Table S2). This indicates that the event was governed mainly by hygroscopic growth and nitrate accumulation, rather than by strong oxidative ROS production. High RH and ALWC favor heterogeneous N_2O_5 hydrolysis and HNO_3 partitioning, promoting rapid nitrate build-up and aerosol mass enhancement (Liu et al., 2020; Zang et al., 2022). However, weak autumn photochemistry and efficient radical termination under high- NO_x/HNO_3 conditions likely limited peroxide formation and suppressed ROS_g accumulation (Tan et al., 2018; Ye et al., 2025). Meanwhile, elevated aerosol water may also accelerate multiphase peroxide loss and organic peroxide decomposition, preventing ROS_p from increasing despite substantial particle growth (Xuan et al., 2020). Thus, autumn represents a high-mass but weakly oxidative regime, where nitrate-water amplification outweighed ROS production. Trajectory clustering indicates that polluted days were dominated by westerly air masses (~41%), with additional southerly (~28%) and easterly (~16%) influence (Figure S5a), consistent with regionally confined transport and limited ventilation over the Beijing-Hebei region. During the clean-up stage, the airflow shifted toward more ventilated northerly (~43%) and southwesterly (~24%) pathways (Figure S5b), favoring pollutant dispersion and the decline of ROS.

The spring pollution episode was an O_3 -dominated event, with mean O_3 reaching 104.74 ppbv, while ALWC and secondary inorganic aerosol levels were lower than in autumn (Figure 8). In contrast to autumn, ROS_g increased markedly from 2.10 to 3.02 ppbv, whereas ROS_p remained relatively stable at about 0.45 $\mu g m^{-3}$ (Table S2). This pattern indicates that spring pollution was controlled mainly by intensified gas-phase photochemistry rather than aerosol aqueous processing. High- O_3 conditions generally reflect strong atmospheric oxidation capacity, sustained by O_3 photolysis, HONO photolysis, and active HO_x cycling, all of which favor the formation of peroxides and other ROS_g (Tan et al., 2019; Ye et al., 2025). The limited change in ROS_p indicates that ROS_p was less sensitive to oxidant abundance alone and more constrained by aerosol composition and SOA aging processes (Zhou et al., 2019). Therefore, spring can be interpreted as a photochemically active gas-phase oxidation



regime, characterized by efficient ROS_g production but only moderate ROS_p enhancement. Spring trajectories were dominated
475 by southerly to southeasterly transport ($\sim 81\%$), with minor northeasterly ($\sim 9\%$) and westerly ($\sim 8\%$) contributions (Figure S5c),
indicating persistent precursor import from the North China Plain. During the clean-up stage, the contribution of northwesterly
and northerly inflow increased ($\sim 24\%$ and $\sim 23\%$), while the southern sector decreased to $\sim 28\%$ (Figure S5d), consistent with
weaker precursor supply, stronger ventilation, and the coherent decline of O_3 and ROS.

Summer showed the clearest decoupling between aerosol mass and ROS behavior (Figure 8). Although $PM_{2.5}$ varied only
480 slightly ($23.5\text{--}27.5\ \mu\text{g m}^{-3}$), and both ALWC and secondary inorganic ions were the lowest of the three seasons, ROS_p increased
substantially from 0.24 to $0.41\ \mu\text{g m}^{-3}$, whereas ROS_g rose only slightly from 1.04 to 1.29 ppbv (Table S2). This pattern
suggests that summertime ROS chemistry was controlled mainly by photochemical aging of organic aerosol rather than by
bulk particle loading. Strong radiation and high temperature enhance VOCs oxidation and O_3 formation, promoting the
generation of more oxidized organic aerosol that can sustain elevated ROS_p even under relatively low PM and inorganic ion
485 levels (Zhou et al., 2019; Zhu et al., 2020). More acidic summer aerosols may further facilitate acid-catalyzed SOA processing
and associated ROS_p formation (Wei et al., 2022). In addition, intense solar radiation can activate photo-initiated heterogeneous
pathways that further enhance particle oxidative activity. Laboratory studies have demonstrated that visible-light irradiation
of soot microstructures can directly generate ROS on particle surfaces, providing an additional photochemical source of ROS_p
in strongly illuminated environments (Zhu et al., 2021). By contrast, the modest increase in ROS_g indicates rapid turnover
490 rather than substantial accumulation of ROS_g in summer. With strong photochemistry and relatively low $PM_{2.5}$, oxidation was
manifested more in efficient O_3 production and continued aerosol aging than in a pronounced enhancement of ROS_g . In this
sense, summer represents an O_3 -rich and organic-oxidation-dominated regime, where aerosol composition, together with
enhanced acidity, rather than aerosol mass, played the key role in determining ROS_p . Trajectory clusters show that polluted
days were dominated by northerly transport (Figure S5e), suggesting the influence of photochemically aged, O_3 -enriched air
495 masses under weak NO titration. During the clean-up stage, southeasterly inflow became dominant, led by a maritime branch
($\sim 32\%$) and additional southeast pathways ($\sim 23\%$) (Figure S5f), providing cleaner ventilation and driving the rapid decline of
 O_3 and ROS.

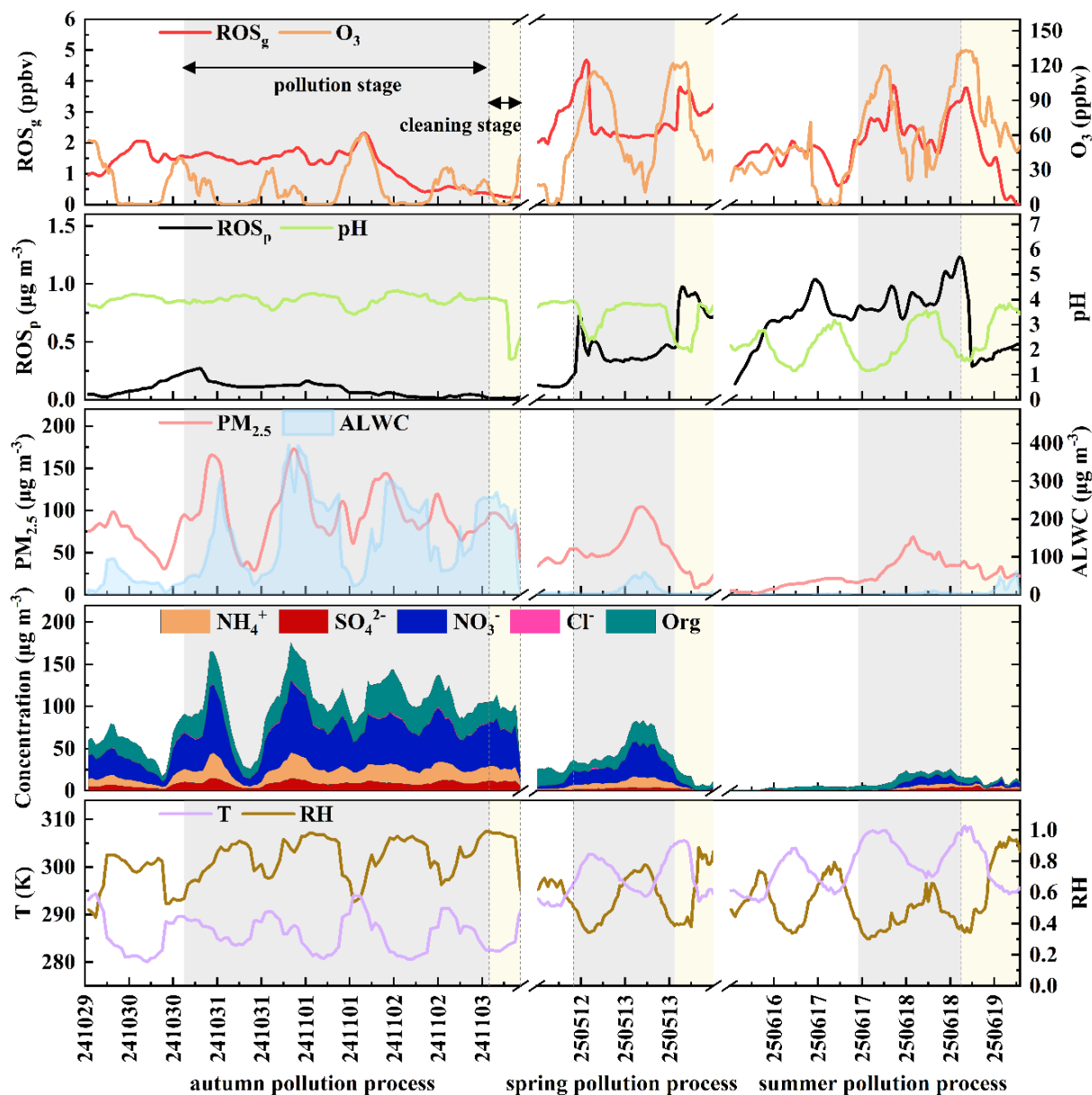


Figure 9. Typical pollution processes observed in different seasons

500 5. Conclusions

This study developed an integrated online analyzer for synchronous quantification of ROS_g and ROS_p . It employs phase-resolved, mild wet-chemical sampling: ROS_g is absorbed via a glass spiral absorption tube, while ROS_p is collected after gas stripping by a rotating wet denuder, using an ambient-temperature spray growth collection chamber to prevent thermal



decomposition. The analysis is performed via online mixing with DCFH and HRP reagents, where HRP catalyzes ROS
505 oxidation of DCFH to fluorescent DCF. Fluorescence intensity (470/520 nm) is measured by a compact LED-PMT module,
with data acquired in real-time via a LabVIEW system. The instrument achieved high stability (RSD 0.37% over 10 h), rapid
response ($T_{90} = 7$ min), low detection limits (0.07 ppbv for ROS_g ; $0.006 \mu\text{g m}^{-3}$ for ROS_p), robust linearity ($y \approx 0.1x$, $R^2 = 0.99$),
and good repeatability (RSD 0.57%, $n = 10$).

Four-season observations in Beijing showed that ROS variability was strongly controlled by pollution regime and
510 photochemical intensity. Seasonal mean ROS_g and ROS_p both peaked in spring and were lowest in autumn. In humid, $PM_{2.5}$ -
dominated autumn haze, high aerosol water and secondary inorganic accumulation were accompanied by only limited ROS
enhancement, implying that condensed-phase turnover and loss restricted net ROS_p buildup. By contrast, O_3 -driven spring and
summer pollution promoted stronger photochemistry, tighter gas-particle coupling, and concurrent increases in ROS_g and
 ROS_p , with summer showing especially strong particle-phase enhancement. The coherent decline of both phases during clean-
515 up stages further indicates that ROS provides a sensitive indicator of coupled changes in oxidant production, partitioning,
transport, and removal.

Data availability

Data related to this article are available online at <https://doi.org/10.5281/zenodo.19446597>.

Supplement link

520 The link to the supplement will be included by Copernicus, if applicable.

Author contributions

Yihui Wang: technology ROS analyzer, conceptualization, formal analysis, investigation, methodology, writing (original draft
preparation), writing (review and editing); Song Huan: formal analysis, investigation, methodology; Huabin Dong:
investigation, methodology; Shiyi Chen: investigation, methodology; Linghan Zeng: conceptualization, investigation,
525 methodology, writing (review and editing); Keding Lu: conceptualization, funding acquisition, project administration, writing
(review and editing).

Competing interests

Keding Lu is a member of the editorial board of Atmospheric Measurement Techniques. The authors have no other competing
interests to declare.



530 Acknowledgements

This work was supported by the National Natural Science Foundation of China (grants.22325601, 42475110, and 22406003).

Financial support

This work was supported by the National Natural Science Foundation of China (grant 22325601, 42475110, and 22406003).

References

- 535 Abdulaal, W. H., Almulaiky, Y. Q., and El-Shishtawy, R. M.: Encapsulation of HRP enzyme onto a magnetic Fe₃O₄ Np-PMMA film via casting with sustainable biocatalytic activity, *Catalysts*, 10, 181, <https://doi.org/10.3390/catal10020181>, 2020.
- Allegri, I., De Santis, F., Di Palo, V., Febo, A., Perrino, C., Possanzini, M., and Liberti, A.: Annular denuder method for sampling reactive gases and aerosols in the atmosphere, *Science of the Total Environment*, 67, 1-16, [https://doi.org/10.1016/0048-9697\(87\)90062-3](https://doi.org/10.1016/0048-9697(87)90062-3), 1987.
- 540 An, Z., Huang, R.-J., Zhang, R., Tie, X., Li, G., Cao, J., Zhou, W., Shi, Z., Han, Y., and Gu, Z.: Severe haze in northern China: A synergy of anthropogenic emissions and atmospheric processes, *Proceedings of the National Academy of Sciences*, 116, 8657-8666, <https://doi.org/10.1073/pnas.1900125116>, 2019.
- Bates, J. T., Weber, R. J., Abrams, J., Verma, V., Fang, T., Klein, M., Strickland, M. J., Sarnat, S. E., Chang, H. H., and Mulholland, J. A.: Reactive oxygen species generation linked to sources of atmospheric particulate matter and cardiorespiratory effects, *Environmental science & technology*, 49, 13605-13612, <https://doi.org/10.1021/acs.est.5b02967>, 2015.
- 545 Bielski, B. H., Shiue, G. G., and Bajuk, S.: Reduction of nitro blue tetrazolium by CO₂-and O₂-radicals, *The Journal of Physical Chemistry*, 84, 830-833, <https://doi.org/10.1021/j100445a006>, 1980.
- Birks, J.: Fluorescence quantum yield measurements, *Journal of research of the National Bureau of Standards. Section A, Physics and chemistry*, 80, 389, <https://doi.org/10.6028/jres.080A.038>, 1976.
- 550 Brown, S. S. and Stutz, J.: Nighttime radical observations and chemistry, *Chemical Society Reviews*, 41, 6405-6447, <https://doi.org/10.1039/C2CS35181A>, 2012.
- Campbell, S. J., Wolfer, K., Utiger, B., Westwood, J., Zhang, Z.-H., Bukowiecki, N., Steimer, S. S., Vu, T. V., Xu, J., and Straw, N.: Atmospheric conditions and composition that influence PM_{2.5} oxidative potential in Beijing, China, *Atmospheric chemistry and physics*, 21, 5549-5573, <https://doi.org/10.5194/acp-21-5549-2021>, 2021.
- 555 Campos, T. L. and Kok, G. L.: Evaluation of Horibe traps for cryogenic collection of hydrogen peroxide and methyl hydroperoxide, *Atmospheric Environment*, 30, 2575-2582, [https://doi.org/10.1016/1352-2310\(95\)00446-7](https://doi.org/10.1016/1352-2310(95)00446-7), 1996.
- Charrier, J. G. and Anastasio, C.: On dithiothreitol (DTT) as a measure of oxidative potential for ambient particles: evidence for the importance of soluble transition metals, *Atmospheric chemistry and physics (Print)*, 12, 11317, <http://doi.org/10.5194/acpd-12-11317-2012>, 2012.
- 560



- Chen, X., Hopke, P. K., and Carter, W. P.: Secondary organic aerosol from ozonolysis of biogenic volatile organic compounds: chamber studies of particle and reactive oxygen species formation, *Environmental science & technology*, 45, 276-282, <https://doi.org/10.1021/es102166c>, 2011.
- 565 D'Errico, G., Vitiello, G., De Tommaso, G., Abdel-Gawad, F. K., Brundo, M. V., Ferrante, M., De Maio, A., Trocchia, S., Bianchi, A. R., and Ciarcia, G.: Electron Spin Resonance (ESR) for the study of Reactive Oxygen Species (ROS) on the isolated frog skin (*Pelophylax bergeri*): A non-invasive method for environmental monitoring, *Environmental Research*, 165, 11-18, <https://doi.org/10.1016/j.envres.2018.03.044>, 2018.
- Dong, H. B., Zeng, L. M., Hu, M., Wu, Y. S., Zhang, Y. H., Slanina, J., Zheng, M., Wang, Z. F., and Jansen, R.: The application of an improved gas and aerosol collector for ambient air pollutants in China, *Atmospheric Chemistry and Physics*, 12, 10519-10533, <https://doi.org/10.5194/acp-12-10519-2012>, 2012.
- 570 Draxler, R. R. and Hess, G.: Description of the HYSPLIT4 modeling system, 1997.
- Draxler, R. R. and Hess, G.: An overview of the HYSPLIT_4 modelling system for trajectories, *Australian meteorological magazine*, 47, 295-308, <https://doi.org/10.1071/ES98032>, 1998.
- Eftekhari, A., Fortenberry, C. F., Williams, B. J., Walker, M. J., Dang, A., Pfaff, A., Ercal, N., and Morrison, G. C.: Continuous measurement of reactive oxygen species inside and outside of a residential house during summer, *Indoor Air*, 31, 1199-1216, <https://doi.org/10.1111/ina.12789>, 2021.
- 575 Enami, S.: Fates of organic hydroperoxides in atmospheric condensed phases, *The Journal of Physical Chemistry A*, 125, 4513-4523, <https://doi.org/10.1021/acs.jpca.1c01513>, 2021.
- Ervens, B., Herckes, P., Feingold, G., Lee, T., Collett, J., and Kreidenweis, S.: On the drop-size dependence of organic acid and formaldehyde concentrations in fog, *Journal of Atmospheric Chemistry*, 46, 239-269, <https://doi.org/10.1023/A:1026393805907>, 2003.
- 580 Fountoukis, C. and Nenes, A.: ISORROPIA II: a computationally efficient thermodynamic equilibrium model for K^+ - Ca^{2+} - Mg^{2+} - NH_4^+ - Na^+ - SO_4^{2-} - NO_3^- - Cl^- - H_2O aerosols, *Atmospheric Chemistry and Physics*, 7, 4639-4659, <https://doi.org/10.5194/acp-7-4639-2007>, 2007.
- 585 Fuchs, H., Holland, F., and Hofzumahaus, A.: Measurement of tropospheric RO_2 and HO_2 radicals by a laser-induced fluorescence instrument, *Review of scientific instruments*, 79, 084104-084104-084112, 10.1063/1.2968712, <https://doi.org/10.1063/1.2968712>, 2008.
- Fuller, S., Wragg, F., Nutter, J., and Kalberer, M.: Comparison of on-line and off-line methods to quantify reactive oxygen species (ROS) in atmospheric aerosols, *Atmospheric Environment*, 92, 97-103, <https://doi.org/10.1016/j.atmosenv.2014.04.006>, 2014.
- 590 George, I., Matthews, P., Whalley, L., Brooks, B., Goddard, A., Baeza-Romero, M., and Heard, D.: Measurements of uptake coefficients for heterogeneous loss of HO_2 onto submicron inorganic salt aerosols, *Physical Chemistry Chemical Physics*, 15, 12829-12845, <https://doi.org/10.1039/C3CP51831K>, 2013.
- Guo, X., Gong, D., Li, J., Mo, X., Ding, X., Chen, J., Chen, X., Li, X., He, Y., and Wang, L.: Comprehensive measurement of carbonyls in Lhasa, Tibetan Plateau: Implications for strong atmospheric oxidation capacity, *Science of The Total Environment*, 948, 174626, <https://doi.org/10.1016/j.scitotenv.2024.174626>, 2024.



- He, C., Lu, X., Wang, H., Wang, H., Li, Y., He, G., He, Y., Wang, Y., Zhang, Y., and Liu, Y.: The unexpected high frequency of nocturnal surface ozone enhancement events over China: characteristics and mechanisms, *Atmospheric Chemistry and Physics*, 22, 15243-15261, <https://doi.org/10.5194/acp-22-15243-2022>, 2022.
- 600 Hellpointner, E. and Gäb, S.: Detection of methyl, hydroxymethyl and hydroxyethyl hydroperoxides in air and precipitation, *Nature*, 337, 631-634, <https://doi.org/10.1038/337631a0>, 1989.
- Hua, W., Chen, Z., Jie, C., Kondo, Y., Hofzumahaus, A., Takegawa, N., Chang, C., Lu, K., Miyazaki, Y., and Kita, K.: Atmospheric hydrogen peroxide and organic hydroperoxides during PRIDE-PRD'06, China: their concentration, formation mechanism and contribution to secondary aerosols, *Atmospheric Chemistry and Physics*, 8, 6755-6773, 605 <https://doi.org/10.5194/acp-8-6755-2008>, 2008.
- Huang, W., Zhang, Y., Zhang, Y., Zeng, L., Dong, H., Huo, P., Fang, D., and Schauer, J. J.: Development of an automated sampling-analysis system for simultaneous measurement of reactive oxygen species (ROS) in gas and particle phases: GAC-ROS, *Atmospheric environment*, 134, 18-26, <https://doi.org/10.1016/j.atmosenv.2016.03.038>, 2016.
- 610 Hung, H.-F. and Wang, C.-S.: Experimental determination of reactive oxygen species in Taipei aerosols, *Journal of Aerosol Science*, 32, 1201-1211, [https://doi.org/10.1016/S0021-8502\(01\)00051-9](https://doi.org/10.1016/S0021-8502(01)00051-9), 2001.
- Ivanova, I. A., Ershova, M. O., Shumov, I. D., Valueva, A. A., Ivanov, Y. D., and Pleshakova, T. O.: Atomic Force Microscopy Study of the Temperature and Storage Duration Dependencies of Horseradish Peroxidase Oligomeric State, *Biomedicines*, 10, 2645, <https://doi.org/10.3390/biomedicines10102645>, 2022.
- 615 Jambunathan, N.: Determination and detection of reactive oxygen species (ROS), lipid peroxidation, and electrolyte leakage in plants, *Plant stress tolerance: methods and protocols*, 291-297, https://doi.org/10.1007/978-1-60761-702-0_18, 2010.
- Keenan, C. R., Goth-Goldstein, R., Lucas, D., and Sedlak, D. L.: Oxidative stress induced by zero-valent iron nanoparticles and Fe (II) in human bronchial epithelial cells, *Environmental Science & Technology*, 43, 4555-4560, <https://doi.org/10.1021/es9006383>, 2009.
- 620 King, L. E. and Weber, R. J.: Development and testing of an online method to measure ambient fine particulate reactive oxygen species (ROS) based on the 2', 7'-dichlorofluorescein (DCFH) assay, *Atmospheric Measurement Techniques*, 6, 1647-1658, <https://doi.org/10.5194/amt-6-1647-2013>, 2013.
- Komazaki, Y., Inoue, T., and Tanaka, S.: Automated measurement system for H₂O₂ in the atmosphere by diffusion scrubber sampling and HPLC analysis of Ti (IV)-PAR-H₂O₂ complex, *Analyst*, 126, 587-593, <https://doi.org/10.1039/B008134P>, 2001.
- 625 Kroll, J. H., Ng, N. L., Murphy, S. M., Flagan, R. C., and Seinfeld, J. H.: Secondary organic aerosol formation from isoprene photooxidation, *Environmental science & technology*, 40, 1869-1877, <https://doi.org/10.1021/es0524301>, 2006.
- Lahey, P. S., Berkemeier, T., Tong, H., Arangio, A. M., Lucas, K., Pöschl, U., and Shiraiwa, M.: Chemical exposure-response relationship between air pollutants and reactive oxygen species in the human respiratory tract, *Scientific reports*, 6, 32916, <https://doi.org/10.1038/srep32916>, 2016.
- 630 Lazrus, A. L., Kok, G. L., Lind, J. A., Gitlin, S. N., Heikes, B. G., and Shetter, R. E.: Automated fluorometric method for hydrogen peroxide in air, *Analytical chemistry*, 58, 594-597, <https://doi.org/10.1021/ac00294a024>, 1986.
- LeBel, C. P., Ischiropoulos, H., and Bondy, S. C.: Evaluation of the probe 2', 7'-dichlorofluorescein as an indicator of reactive oxygen species formation and oxidative stress, *Chemical research in toxicology*, 5, 227-231, <https://doi.org/10.1021/tx00026a012>, 1992.



- 635 Lee, J. H., Tang, I. N., and Weinstein-Lloyd, J. B.: A non-enzymatic method for the determination of hydrogen peroxide in atmospheric samples, *Analytical Chemistry*, 62, 2381-2384, <https://doi.org/10.1021/ac00220a022>, 1990.
- Lee, M., Noone, B. C., O'sullivan, D., and Heikes, B. G.: Method for the Collection and HPLC Analysis of Hydrogen Peroxide and C 1 and C 2 Hydroperoxides in the Atmosphere, *Journal of Atmospheric and Oceanic Technology*, 12, 1060-1070, [https://doi.org/10.1175/1520-0426\(1995\)012<1060:MFTCAH>2.0.CO;2](https://doi.org/10.1175/1520-0426(1995)012<1060:MFTCAH>2.0.CO;2), 1995.
- 640 Lelieveld, J. a., Butler, T. M., Crowley, J. N., Dillon, T. J., Fischer, H., Ganzeveld, L., Harder, H., Lawrence, M. G., Martinez, M., and Taraborrelli, D.: Atmospheric oxidation capacity sustained by a tropical forest, *Nature*, 452, 737-740, <https://doi.org/10.1038/nature06870>, 2008.
- Li, H., Zhang, Q., Zheng, B., Chen, C., Wu, N., Guo, H., Zhang, Y., Zheng, Y., Li, X., and He, K.: Nitrate-driven urban haze pollution during summertime over the North China Plain, *Atmospheric Chemistry and Physics*, 18, 5293-5306, <https://doi.org/10.5194/acp-18-5293-2018>, 2018.
- 645 Liu, P., Ye, C., Xue, C., Zhang, C., Mu, Y., and Sun, X.: Formation mechanisms of atmospheric nitrate and sulfate during the winter haze pollution periods in Beijing: gas-phase, heterogeneous and aqueous-phase chemistry, *Atmospheric Chemistry and Physics*, 20, 4153-4165, <https://doi.org/10.5194/acp-20-4153-2020>, 2020.
- Liu, Y., Tang, X., Zhang, Z., Li, L., and Chen, J.: Development and Field Testing of an Online Monitoring System for Atmospheric Particle-Bound Reactive Oxygen Species (ROS), *Atmosphere*, 14, 924, <https://doi.org/10.3390/atmos14060924>,
650 2023.
- Liu, Z., Wang, Y., Hu, B., Lu, K., Tang, G., Ji, D., Yang, X., Gao, W., Xie, Y., and Liu, J.: Elucidating the quantitative characterization of atmospheric oxidation capacity in Beijing, China, *Science of the Total Environment*, 771, 145306, <https://doi.org/10.1016/j.scitotenv.2021.145306>, 2021.
- Lushchak, V. I. and Lushchak, O.: Interplay between reactive oxygen and nitrogen species in living organisms, *Chemico-Biological Interactions*, 349, 109680, <https://doi.org/10.1016/j.cbi.2021.109680>, 2021.
- 655 Montesinos, V. N., Sleiman, M., Cohn, S., Litter, M. I., and Destailhats, H.: Detection and quantification of reactive oxygen species (ROS) in indoor air, *Talanta*, 138, 20-27, <https://doi.org/10.1016/j.talanta.2015.02.015>, 2015.
- Mrakic-Sposta, S., Gussoni, M., Montorsi, M., Porcelli, S., and Vezzoli, A.: Assessment of a standardized ROS production profile in humans by electron paramagnetic resonance, *Oxidative Medicine and Cellular Longevity*, 2012, 973927, <https://doi.org/10.1155/2012/973927>, 2012.
- 660 Murakami, Y., Endo, K., Ohta, I., Nosaka, A. Y., and Nosaka, Y.: Can OH radicals diffuse from the UV-irradiated photocatalytic TiO₂ surfaces? Laser-induced-fluorescence study, *The Journal of Physical Chemistry C*, 111, 11339-11346, <https://doi.org/10.1021/jp0722049>, 2007.
- Nan, J., Wang, S., Guo, Y., Xiang, Y., and Zhou, B.: Study on the daytime OH radical and implication for its relationship with fine particles over megacity of Shanghai, China, *Atmospheric Environment*, 154, 167-178, <https://doi.org/10.1016/j.atmosenv.2017.01.046>, 2017.
- Nosaka, Y. and Nosaka, A. Y.: Generation and detection of reactive oxygen species in photocatalysis, *Chemical reviews*, 117, 11302-11336, <https://doi.org/10.1021/acs.chemrev.7b00161>, 2017.



- 670 Olaguer, E. P., Rappenglück, B., Lefer, B., Stutz, J., Dibb, J., Griffin, R., Brune, W. H., Shauck, M., Buhr, M., and Jeffries, H.: Deciphering the role of radical precursors during the Second Texas Air Quality Study, *Journal of the Air & Waste Management Association*, 59, 1258-1277, <https://doi.org/10.3155/1047-3289.59.11.1258>, 2009.
- Sakugawa, H. and Kaplan, I. R.: Atmospheric H₂O₂ measurement: comparison of cold trap method with impinger bubbling method, *Atmospheric Environment* (1967), 21, 1791-1798, [https://doi.org/10.1016/0004-6981\(87\)90119-3](https://doi.org/10.1016/0004-6981(87)90119-3), 1987.
- 675 Scott, C., Rap, A., Spracklen, D., Forster, P., Carslaw, K., Mann, G., Pringle, K., Kivekäs, N., Kulmala, M., and Lihavainen, H.: The direct and indirect radiative effects of biogenic secondary organic aerosol, *Atmospheric Chemistry and Physics*, 14, 447-470, <https://doi.org/10.5194/acp-14-447-2014>, 2014.
- Shiraiwa, M. and Pöschl, U.: Mass accommodation and gas-particle partitioning in secondary organic aerosols: dependence on diffusivity, volatility, particle-phase reactions, and penetration depth, *Atmospheric Chemistry and Physics*, 21, 1565-1580, <https://doi.org/10.5194/acp-21-1565-2021>, 2021.
- 680 Simões, E. F., Almeida, A. S., Duarte, A. C., and Duarte, R. M.: Assessing reactive oxygen and nitrogen species in atmospheric and aquatic environments: Analytical challenges and opportunities, *TrAC Trends in Analytical Chemistry*, 135, 116149, <https://doi.org/10.1016/j.trac.2020.116149>, 2021.
- 685 Song, L., Yin, S., Bi, S., Yang, J., Wang, X., Bi, X., Zhang, Y., Wu, J., Dai, Q., and Feng, Y.: More evidence on primary sulfate emission from residential coal combustion in northern China: Insights from the size-segregated chemical profile, morphology, and sulfur isotope, *Atmospheric Environment*, 326, 120467, <https://doi.org/10.1016/j.atmosenv.2024.120467>, 2024.
- Stein, A. F., Draxler, R. R., Rolph, G. D., Stunder, B. J., Cohen, M. D., and Ngan, F.: NOAA's HYSPLIT atmospheric transport and dispersion modeling system, *Bulletin of the American Meteorological Society*, 96, 2059-2077, <https://doi.org/10.1175/BAMS-D-14-00110.1>, 2015.
- 690 Stone, D., Whalley, L. K., and Heard, D. E.: Tropospheric OH and HO₂ radicals: field measurements and model comparisons, *Chemical Society Reviews*, 41, 6348-6404, <http://doi.org/10.1039/C2CS35140D>, 2012.
- Tan, Z., Lu, K., Jiang, M., Su, R., Wang, H., Lou, S., Fu, Q., Zhai, C., Tan, Q., and Yue, D.: Daytime atmospheric oxidation capacity in four Chinese megacities during the photochemically polluted season: a case study based on box model simulation, *Atmospheric Chemistry and Physics*, 19, 3493-3513, <https://doi.org/10.5194/acp-19-3493-2019>, 2019.
- 695 Tan, Z., Rohrer, F., Lu, K., Ma, X., Bohn, B., Broch, S., Dong, H., Fuchs, H., Gkatzelis, G. I., and Hofzumahaus, A.: Wintertime photochemistry in Beijing: observations of RO_x radical concentrations in the North China Plain during the BEST-ONE campaign, *Atmospheric Chemistry and Physics*, 18, 12391-12411, <https://doi.org/10.5194/acp-18-12391-2018>, 2018.
- 700 Tanner, R. L., Markovits, G. Y., Ferreri, E. M., and Kelly, T. J.: Sampling and determination of gas-phase hydrogen peroxide following removal of ozone by gas-phase reaction with nitric oxide, *Analytical Chemistry*, 58, 1857-1865, <https://doi.org/10.1021/ac00121a056>, 1986.
- Venkatachari, P. and Hopke, P. K.: Development and laboratory testing of an automated monitor for the measurement of atmospheric particle-bound reactive oxygen species (ROS), *Aerosol Science and Technology*, 42, 629-635, <https://doi.org/10.1080/02786820802227345>, 2008.
- 705 Venkatachari, P., Hopke, P. K., Brune, W. H., Ren, X., Leshner, R., Mao, J., and Mitchell, M.: Characterization of wintertime reactive oxygen species concentrations in Flushing, New York, *Aerosol Science and Technology*, 41, 97-111, <https://doi.org/10.1080/02786820601116004>, 2007.



- Wang, D., Yang, X., Lu, H., Li, D., Xu, H., Luo, Y., Sun, J., Ho, S. S. H., and Shen, Z.: Oxidative potential of atmospheric brown carbon in six Chinese megacities: Seasonal variation and source apportionment, *Atmospheric Environment*, 309, 119909, <https://doi.org/10.1016/j.atmosenv.2023.119909>, 2023a.
- 710 Wang, Y., Bagya Ramesh, C., Giangrande, S. E., Fast, J., Gong, X., Zhang, J., Tolga Odabasi, A., Oliveira, M. V. B., Matthews, A., and Mei, F.: Examining the vertical heterogeneity of aerosols over the Southern Great Plains, *Atmospheric chemistry and physics*, 23, 15671-15691, <https://doi.org/10.5194/acp-23-15671-2023>, 2023b.
- Wang, Y., Jin, X., Liu, Z., Wang, G., Tang, G., Lu, K., Hu, B., Wang, S., Li, G., and An, X.: Progress in quantitative research on the relationship between atmospheric oxidation and air quality, *Journal of Environmental Sciences*, 123, 350-366, 715 <https://doi.org/10.1016/j.jes.2022.06.029>, 2023c.
- Wang, Y., Zhang, Q., Jiang, J., Zhou, W., Wang, B., He, K., Duan, F., Zhang, Q., Philip, S., and Xie, Y.: Enhanced sulfate formation during China's severe winter haze episode in January 2013 missing from current models, *Journal of Geophysical Research: Atmospheres*, 119, 10,425-410,440, <https://doi.org/10.1002/2013JD021426>, 2014.
- Wei, J., Fang, T., and Shiraiwa, M.: Effects of acidity on reactive oxygen species formation from secondary organic aerosols, 720 *ACS environmental Au*, 2, 336-345, <https://doi.org/10.1021/acsenvironau.2c00018>, 2022.
- Wennberg, P. O., Bates, K. H., Crouse, J. D., Dodson, L. G., McVay, R. C., Mertens, L. A., Nguyen, T. B., Praske, E., Schwantes, R. H., and Smarte, M. D.: Gas-phase reactions of isoprene and its major oxidation products, *Chemical reviews*, 118, 3337-3390, <https://doi.org/10.1021/acs.chemrev.7b00439>, 2018.
- Wu, J., Yang, C., Zhang, C., Cao, F., Wu, A., and Zhang, Y.: Development, characterization, and application of an improved 725 online reactive oxygen species analyzer based on the Monitor for AeRosols and Gases in ambient Air (MARGA), *Atmospheric Measurement Techniques*, 15, 2623-2633, <https://doi.org/10.5194/amt-15-2623-2022>, 2022.
- Xie, Z. H., He, C. S., Pei, D. N., Dong, Y., Yang, S. R., Xiong, Z. K., Zhou, P., Pan, Z. C., Yao, G., and Lai, B.: Review of characteristics, generation pathways and detection methods of singlet oxygen generated in advanced oxidation processes (AOPs), *Chemical Engineering Journal*, 468, 143778, <https://doi.org/10.1016/j.cej.2023.143778>, 2023.
- 730 Xuan, X., Chen, Z., Gong, Y., Shen, H., and Chen, S.: Partitioning of hydrogen peroxide in gas-liquid and gas-aerosol phases, *Atmospheric Chemistry and Physics*, 20, 5513-5526, <https://doi.org/10.5194/acp-20-5513-2020>, 2020.
- Xue, C., Ye, C., Kleffmann, J., Zhang, W., He, X., Liu, P., Zhang, C., Zhao, X., Liu, C., and Ma, Z.: Atmospheric 735 Measurements at the Foot and the Summit of Mt. Tai—Part II: HONO Budget and Radical ($\text{RO}_x + \text{NO}_3$) Chemistry in the Lower Boundary Layer, *Atmospheric Chemistry and Physics Discussions*, 2021, 1-36, <https://doi.org/10.5194/acp-22-3149-2022>, 2021.
- Yang, J., Cao, Y., and Zhang, N.: Spectrophotometric method for superoxide anion radical detection in a visible light (400–780 nm) system, *Spectrochimica Acta Part A: Molecular and Biomolecular Spectroscopy*, 239, 118556, <https://doi.org/10.1016/j.saa.2020.118556>, 2020.
- 740 Yao, L., Ma, Y., Wang, L., Zheng, J., Khalizov, A., Chen, M., Zhou, Y., Qi, L., and Cui, F.: Role of stabilized Criegee Intermediate in secondary organic aerosol formation from the ozonolysis of α -cedrene, *Atmospheric Environment*, 94, 448-457, <https://doi.org/10.1016/j.atmosenv.2014.05.063>, 2014.
- Ye, C., Liu, P., Xue, C., Zhang, C., Ma, Z., Liu, C., Liu, J., Lu, K., Mu, Y., and Zhang, Y.: Understanding summertime H_2O_2 chemistry in the North China Plain through observations and modeling studies, *Atmospheric Chemistry and Physics*, 25, 6991-7005, <https://doi.org/10.5194/acp-25-6991-2025>, 2025.



- 745 Ying, N., Tang, Y., Wang, D., Fan, J., Zhao, Z., Xue, Z., and Liu, Y.: Detecting atmospheric oxidation in the PM_{2.5} and ozone multilayer complex network, *Environmental Research Letters*, 19, 104072, <http://doi.org/10.1088/1748-9326/ad7869>, 2024.
- Yu, W. and Zhao, L.: Chemiluminescence detection of reactive oxygen species generation and potential environmental applications, *TrAC Trends in Analytical Chemistry*, 136, 116197, <https://doi.org/10.1016/j.trac.2021.116197>, 2021.
- 750 Zang, H., Zhao, Y., Huo, J., Zhao, Q., Fu, Q., Duan, Y., Shao, J., Huang, C., An, J., and Xue, L.: High atmospheric oxidation capacity drives wintertime nitrate pollution in the eastern Yangtze River Delta of China, *Atmospheric Chemistry and Physics*, 22, 4355-4374, <https://doi.org/10.5194/acp-22-4355-2022>, 2022.
- Zhang, G., Hu, R., Xie, P., Cai, H., Shen, C., Guo, J., Hu, C., and Liu, X.: Improved laser-induced fluorescent instrument for online peroxy radical measurement: Consistency in high-sensitivity for detection, *Sensors and actuators. B, Chemical*, 424, 136774, 10.1016/j.snb.2024.136774, <https://doi.org/10.1016/j.snb.2024.136774>, 2025.
- 755 Zhang, Y., Dai, M., and Yuan, Z.: Methods for the detection of reactive oxygen species, *Analytical Methods*, 10, 4625-4638, <https://doi.org/10.1039/C8AY01339J>, 2018.
- Zhao, J. and Hopke, P. K.: Concentration of reactive oxygen species (ROS) in mainstream and sidestream cigarette smoke, *Aerosol Science and Technology*, 46, 191-197, <https://doi.org/10.1080/02786826.2011.617795>, 2012.
- 760 Zhou, J., Bruns, E. A., Zotter, P., Stefenelli, G., Prévôt, A. S., Baltensperger, U., El-Haddad, I., and Dommen, J.: Development, characterization and first deployment of an improved online reactive oxygen species analyzer, *Atmospheric Measurement Techniques*, 11, 65-80, <https://doi.org/10.5194/amt-11-65-2018>, 2018.
- Zhou, J., Elser, M., Huang, R.-J., Krapf, M., Fröhlich, R., Bhattu, D., Stefenelli, G., Zotter, P., Bruns, E. A., and Pieber, S. M.: Predominance of secondary organic aerosol to particle-bound reactive oxygen species activity in fine ambient aerosol, *Atmospheric Chemistry and Physics*, 19, 14703-14720, <https://doi.org/10.5194/acp-19-14703-2019>, 2019.
- 765 Zhu, J., Shang, J., and Zhu, T.: A new understanding of the microstructure of soot particles: The reduced graphene oxide-like skeleton and its visible-light driven formation of reactive oxygen species, *Environmental Pollution*, 270, 116079, <https://doi.org/10.1016/j.envpol.2020.116079>, 2021.
- 770 Zhu, J., Wang, S., Wang, H., Jing, S., Lou, S., Saiz-Lopez, A., and Zhou, B.: Observationally constrained modeling of atmospheric oxidation capacity and photochemical reactivity in Shanghai, China, *Atmospheric Chemistry and Physics*, 20, 1217-1232, <https://doi.org/10.5194/acp-20-1217-2020>, 2020.